Electronic Transfer as a Route to Increase the Chemical Stability in Gold and Silver Core-Shell Nanoparticles

Derrick M. Mott*, Dao Thi Ngoc Anh, Prerna Singh, Cheshta Shankar and Shinya Maenosono

Japan Advanced Institute of Science and Technology, School of Materials Science, 1-1 Asahidai, Nomi, Ishikawa 923-1292, Japan

Email: derrickm@jaist.ac.jp
Phone: 81-761-51-1612
Fax: 81-761-51-1149

Abstract

This review article presents the collected recent findings and advancements in understanding and manipulating the electronic properties of the Au/Ag NP system from the standpoint of controlling the characteristics of heterostructured core@shell NPs. The discovery of the electronic transfer effect through analysis of both Ag@Au and Au@Ag type NPs inspired the analysis of the resulting enhanced properties. First, the background on the synthesis and characterization of Ag, Au, Ag@Au, Au@Ag and Au@Ag@Au NPs, which will be used as a basis for studying the electronic transfer and stability properties is presented. Next, Mie Theory is used to inspect the optical properties of the Ag@Au NPs, revealing subtle structural characteristics in these probes, which has implications to the plasmonic properties. This is followed by the inspection of the electronic properties of the Au@Ag NPs primarily through XPS and XANES analysis, revealing the origins of the electronic transfer phenomenon. The unique electronic properties are then revealed to result in improved particle stability in terms of susceptibility to oxidation. Finally, an assessment of the resulting enhanced plasmonic sensing properties is discussed. The results are presented in terms of synthesis technique, material characterization, understanding of the electronic properties and manipulation of those properties to create Au@Ag NPs with enhanced resistance to oxidation and galvanic replacement.

KEYWORDS: Gold, Silver, Core/shell, Electronic Transfer, Plasmonic

CONTENTS

1. INTRODUCTION

Nanotechnology is driven by the desire to discover materials with new, unique and technologically beneficial properties that can be used in advanced applications. Our knowledge in the field has come a long way in a short time, yet there is still much we don't understand about how to control the specific novel properties, which arise as a function of the particle characteristics such as size, shape, composition, structure, surface properties, etc. Gold (Au) and Silver (Ag) Nanoparticles (NPs) are some of the oldest known examples and have received the most attention in terms of synthetic refinement and elucidation of the resulting nanoscale properties. Yet there are still important discoveries being made that provide insight on how to truly control these novel properties, which can be applied to a broad range of NP systems. Much of the knowledge being gained in this area today includes techniques for manipulating the NP structure or composition in multicomponent type NPs. Such systems can display multiple properties arising from the individual components, but it is the observation of synergistic phenomena that is the most intriguing. A good example of this is the Au/platinum (Pt) alloy NP system, where it was found that the isolation of Pt atoms in the Au matrix led to an electronic d-

band shift at the Pt sites, resulting in enhanced methanol oxidation reactivity, which could not be achieved with pure Au or Pt NPs [1]. Building on these types of observed phenomena, researchers have begun to probe increasingly complex NP structures, developing systems where the individual NPs are composed of multiple components, for example the well-known core@shell NP structures [2]. This class of NP has been termed "heterostructured", reflecting the multicomponent nature of the individual NPs. These new NP materials offer multiple parameters that can be individually tuned to manipulate the desired NP properties. Several examples have emerged of promising heterostructured systems that display multifunctional properties arising from the individual components. Heterostructured nanowires (NW)s composed of semiconducting core and shell components such as silicon and germanium have been synthesized which offer the ability to tune the emission or passivation properties of the materials, opening the door to a wide range of photonic and electronic device applications [3]. Tetrapod structured NPs composed of cadmium selenide cores with cadmium sulfide arms have been demonstrated to possess high photoluminescence efficiencies and large extinction coefficients which are promising for bio-diagnostics and bio-molecular labeling applications [4].

Perhaps the most well-known heterostructured NPs include the coinage metal plasmonic NPs. Au and Ag heterostructured NPs are a classic example that illustrates the potential for heterostructures to offer enhanced, synergistic or multi-functionality in a single particle [2]. As a result, a wide range of structures have been synthesized with the target of controlling the optical, reactivity and stability properties [5,6,7]. This class of NP is considered very promising for use in molecular sensing and bio-diagnostics applications where the unique plasmonic properties of the particles serve as a sensitive route to detecting minute traces of analyte or target molecule [8,9]. Ideally speaking, Ag@Au NPs are considered ideal for these applications because the Ag core would supply enhanced plasmonic properties (high extinction coefficient) while a Au shell would impart bio-molecular reactivity (*via* sulfur reactivity) as well as chemical stability against aggregation and oxidation [5,8,9,10,11]. The ability to obtain this structure however, is elusive

because of the relatively higher reduction potential for Au over Ag, resulting in the galvanic replacement reaction [6,7,12,13,14,15]. The end result is typically quasi-core@shell particles that have imperfections such as gaps or holes in the Au shell, alloying, or even complete removal of the Ag core [5,6,7,12,13,14,16,17]. The inverse structure (i.e. Au@Ag) is also interesting, but has traditionally not been considered feasible as a sensing probe because of the exposure of Ag to the outside environment, leading to surface oxidation and NP aggregation. However, it has recently been shown that careful control of the structure in Au@Ag NPs leads to the observation of enhanced properties for the Ag in terms of resisting oxidation and the galvanic replacement reaction [15,18,19,20]. The observation is unexpected because many researchers have probed the properties for this NP heterostructure without observing the enhanced stability [21]. The key to the observation is to control the thickness of the Ag shell in a range where a unique electronic transfer from the Au core to the Ag shell can take place [19,20]. Such a finding is of note not only because of the potential implications to the development of plasmonic sensors, but also because the phenomenon can be applied to other heterostructured NP systems, for example in catalysis, magnetics and thermoelectrics applications, among many others. The complete understanding of the recently discovered charge transfer phenomenon in Au@Ag NPs has the potential to lead to a new class of NPs with unique and novel properties and will provide the necessary insight to develop new and unique materials that are composed of abundant and non-toxic elements for future high technology applications.

2. SYNTHESIS OF CORE@SHELL NANOSTRUCTURES

There is a much literature available on various synthesis techniques towards noble and coinage metal NPs. As is well known, the most important aspect is the ability to control the size, shape, composition, structure and surface properties of the resulting NPs that is of paramount importance. The control of these NP characteristics is key because these are what determine the unique properties that arise as a result of the nanoscale size of the particles. The unique properties of NPs

are oftentimes highly size dependent and the ability to obtain a desired property is directly linked to the ability to control the NP synthesis. While much work has been done elucidating the factors that affect NP characteristics through synthetic means, the work presented here focuses on a narrow slice in the aqueous wet chemical synthesis of Ag and Au based core@shell NPs. These particles serve as a platform to study the resulting unique electronic properties displayed by the core@shell structures, the results of which can be readily applied over the entire field of nanotechnology.

2.0.1. Chemicals used in the Synthesis of NPs. This section lists the chemicals used in the experiments throughout this review. Gold tetrachloroaurate trihydrate ($HAuCl_4 \cdot 3H_2O$) 99.9 %, silver nitrate ($AgNO_3$) 99.9999 %, sodium acrylate (SA) 97 %, trisodium citrate (SC) 99.0 %, sodium chloride (NaCl) 99.0 %, calcium chloride ($CaCl_2$) 96.0 %, hydrochloric acid (HCl) 37 %, and common solvents were obtained from Aldrich. 3-amino-1,2,4-triazole-5-thiol (ATT) 98.0% was obtained from Tokyo Chemical Industry. Water was purified with a Millipore Direct-Q system (18.2 MΩ). 3-aminopropyltrimethoxysilane (APTMS) was obtained from Wako Pure Chemical Industries and was used to functionalize the surface of glass slides as a substrate for Raman analysis. Dialysis membranes with molecular weight pore size of 10,000 daltons were obtained from Spectra/Por and were rinsed in pure water before use.

2.0.2. Instrumentation and Measurements. Techniques including transmission electron microscopy (TEM), High Resolution TEM (HR-TEM), Scanning TEM equipped with a High Angle Annular Dark Field detector (STEM-HAADF), Energy Dispersive Spectroscopy (EDS) elemental mapping, X-Ray Photoelectron Spectroscopy (XPS), Dynamic Light Scattering (DLS), X-Ray Absorption Near Edge Structure (XANES), Raman spectroscopy and Ultraviolet-visible spectroscopy (UV-Vis) were used to characterize the size, shape, composition and other properties of the NPs. TEM analysis was performed on an Hitachi H-7100 instrument operated at 100 kV. HR-TEM and EDS analysis was performed on an Hitachi H-9000NAR transmission electron microscope operated at 300 kV. STEM-HAADF and EDS elemental mapping were

performed on a Jeol JEM-ARM200F operated at 200 kV with a spherical aberration corrector, the nominal resolution is 0.8 Å. Samples for TEM, STEM-HAADF and EDS elemental mapping were prepared by dropping the suspended NPs onto a carbon coated copper grid and drying in air overnight. XPS analysis was carried out on a Shimadzu Kratos AXIS-ULTRA DLD high performance XPS system. Photoelectrons were excited by monochromated Al K_α radiation. Detection was done with a delay-line detector (DLD) and a concentric hemispherical analyzer (CHA). The X-ray tube was operated at 150 W. The pass energy of the CHA was 20 eV for narrow-scan spectra. The analyzed area on the specimen surface was 300×700 μm^2 and was located in the center of the irradiated region. For the sample preparation, the precipitated NPs were deposited on carbon tape and dried in air. The instrument was operated at a vacuum level of 1×10^{-8} Torr. Raman spectra were obtained with an Ar^+ laser (wavelength 514.5 nm, power 50 mW), using a Horiba-Jobin Yvon Ramanor T64000 triple monochromator equipped with a CCD detector. The nonpolarized Raman scattering measurements were set under a microscope sample holder using a 180° backscattering geometry at room temperature. The laser spot diameter was 1 μm. An acquisition time of 60 seconds per spectrum was used with averaging of 3 spectra per analysis area. UV-Vis spectra were collected in the range of 300 to 1100 nm using a Perkin-Elmer Lambda 35 UV-Vis spectrometer.

Au $L_{2,3}$-edge XANES spectra were recorded at beam line BL01B1 of SPring-8 [19]. The photon energy was calibrated by the distinct peak in the differential spectrum of Au foil at the Au L_3-edge as 11.919 keV. The energy step of measurement in the XANES region was 0.3 eV. Both the ion-chambers were filled with N_2(85%)/Ar(15%) (I_0) and Ar (transmission mode), and the Lytle's detector was filled with Kr (fluorescence mode) and was operated at room temperature. NP samples for XANES analysis were adsorbed onto a boehmite (Wako) substrate, diluted with boron nitride (Wako), grained and pressed to a pellet (10 mmϕ). Au foil was used as a reference for the bulk metallic Au. The obtained XANES spectra were analyzed using the Rigaku REX2000 software (ver. 2.5.7). The pre-edge background subtracted spectra were normalized to the edge

jump at the center of EXAFS oscillation following a linear background subtraction, which was taken to the value of the atomic background at 13.815 and 12.050 keV, for the L_2- and L_3-edges, respectively. Estimation of the *d*-orbital electron density was carried out according to Mansour's method [22] as follows; The While Line (WL) feature in the L_2-edge is related to the $2p_{1/2} \rightarrow 5d_{3/2}$ dipole-allowed transition while that of the L_3-edge is due to the $2p_{3/2} \rightarrow 5d_{5/2}$ and $5d_{3/2}$ dipole-allowed transitions, resulting from the spin-orbit interaction of the *d* states [23]. Therefore, integration of these transitions reflects the number of holes in the $5d_{5/2}$ and $5d_{3/2}$ orbitals above the Fermi level as shown in Figure 1A.

Changes in the numbers of holes in the $d_{3/2}$ and $d_{5/2}$ orbitals from those of bulk Au, $\Delta h_{3/2} = h_{3/2,\mathrm{NP}} - h_{3/2,\mathrm{bulk}}$ and $\Delta h_{5/2} = h_{5/2,\mathrm{NP}} - h_{5/2,\mathrm{bulk}}$, were expressed as

$$\Delta h_{3/2} = \frac{3\Delta A_2}{C} \qquad (1)$$

$$\Delta h_{5/2} = \frac{\left(2.25\Delta A_3 - 0.5\Delta A_2\right)}{C} \qquad (2)$$

where $\Delta A_{\mathrm{j}} = A_{\mathrm{j,NP}} - A_{\mathrm{j,bulk}}$ is the difference values between NPs and bulk, and A_{j} is the edge area for the L_{j}-edge XANES spectrum ($\mathrm{eV \cdot cm^{-1}}$). C = 75213 $\mathrm{eV \cdot cm^{-1}}$ is the characteristic constant of the absorption [22,24].

The total width of the WL feature depends on the lifetime of the core hole, the experimental resolution, the dipole-transition matrix element, and the distribution of the density of states of unoccupied *d* band at the Fermi level of the metal [25,26]. However, the first three factors can be considered to be uniform for the $L_{2,3}$-edge WLs [25,26]. To correlate the relative area of the WL to the *d*-electronic structure, the difference spectrum between the L_3- and the L_2-edge XANES spectra of the Au foil was plotted in Figure 1B. A single distinct peak in the

difference spectrum is observed in accordance with previous observations [24]. The area in the range from 10 eV below the X-ray absorption edge (E_0 = 0 eV) to 13 eV above the E_0 was cut off for calculating the *d*-hole density [22]. For the values of $h_{3/2,bulk}$ and $h_{5/2,bulk}$, 0.118 ($atom^{-1}$) and 0.283 ($atom^{-1}$) were used [27]. The occurrence of holes was explained by the spin-orbit splitting and *s*-*p*-*d* hybridization effects [25,27,28,29,30] despite no 5*d* holes in unperturbed Au (electron configuration [Xe]$6s^1 4f^{14} 5d^{10}$).

2.1 Synthesis of Ag NPs

Two types of Ag NPs suspended in water were synthesized as core NPs for the further deposition of Au. Acrylate capped Ag NPs offer high NP size and shape uniformity, which has historically been challenging to achieve with an aqueous synthetic technique. The citrate capped Ag NP synthesis technique offers relatively larger sized Ag NPs as compared to the Acrylate technique at the expense of particle size and shape uniformity.

2.1.1. Synthesis of Acrylate Capped Ag NPs. The ability to synthesize Ag NPs with controllable characteristics such as size, shape and surface properties is still elusive, especially for sensing and bio-diagnostics applications which call for mono-dispersed hydrophilic NPs. The hydrophilic Ag NPs synthesized here are noteworthy for enhanced mono-dispersity in the 20 nm size range [5], and as a result are used as cores for the further deposition of Au in later experiments. Briefly, 50 ml of water was used to dissolve 1.25×10^{-5} moles of $AgNO_3$, and then 6.75×10^{-6} moles of NaOH were slowly added to the solution, which results in a dilute yellow-colored suspension of $Ag(OH)_2^-$ [5]. This solution is purged with argon and is then brought to reflux. At reflux, 2.55×10^{-4} moles of SA are added, causing the suspension to turn completely clear. The solution is refluxed for 1 hour, during which time the color changes from clear to green-yellow and finally to amber-yellow. The as-synthesized Ag NPs were purified before use by the dialysis method. In this approach, NaOH was added, which typically leads to insoluble Ag_2O, a black or brown material. However, the relative concentration of Ag is very low, allowing

the formation of an $Ag(OH)_2^-$ compound [5]. This precursor allows a degree of control over the rate of nucleation and subsequent growth of Ag NPs, which typically is a challenge. In a synthesis where all of the Ag is available from the start of the reaction, as the particles form and grow in size the Ag is used up, changing the Ag precursor concentration and the kinetics of the reaction, which results in non-mono-dispersed NPs. The $Ag(OH)_2^-$ serves as a regulatory source of Ag, resulting in more uniform Ag NPs. Figure 2A shows a TEM image of the as-synthesized Ag NPs capped by acrylate. The particle size distribution is 20.5 ± 3.3 nm (16% deviation) and represents a significant improvement in the mono-dispersity of these particles at this size range over other preparation techniques. UV-Visible spectroscopy in Figure 2B shows the resulting UV-Vis spectrum with an SPR maximum at 416 nm, consistent for Ag NPs. The Ag NP concentration is 7.28×10^{-11} M and the extinction coefficient is $2.11\times10^{10}\,M^{-1}cm^{-1}$ [5].

2.1.2. Synthesis of Citrate Capped Ag NPs. Ag NPs capped in citrate molecules were synthesized to obtain relatively larger Ag NPs [18]. Briefly, 50 ml of a 1 mM solution of $AgNO_3$ was prepared in a 100 ml round flask. This solution is then purged with argon and stirred with heating until reflux. Next, 1 mL of a 3.4×10^{-3} mM aqueous solution of SC is added to the refluxing $AgNO_3$ solution. The solution is refluxed for 1 hour. After about 3 minutes of boiling, the solution turned yellow, and after about 5 minutes it turned gray-yellow and became opaque. The reaction solution was cooled to room temperature after 1 hour of refluxing, the opaque dispersion was then centrifuged at 4000 rpm for 30 minutes. After centrifugation, the upper part of the solution became a transparent yellow color. The upper part of the solution was removed and contains the final citrate capped Ag NPs used in experiments. Figure 3 shows the TEM image and UV-Vis spectrum collected for the as-synthesized NPs, illustrating the general morphology and optical properties. In general the particles have a spherical morphology with a minor fraction of nanorods also being incorporated. The SPR maximum occurs at 403 nm, consistent for Ag NPs, the particle size distribution is 39.4 ± 6.5 nm.

2.2 Synthesis of Au NPs

Two different sizes of Au NPs were prepared using the basic citrate reduction technique [31,32]. These relatively small and large NPs were prepared for two different purposes, the small NPs (~13 nm diameter) are primarily used as cores for the further coating with Ag to create core@shell NPs while the larger Au NPs (~43 nm diameter) are used for comparison of the plasmonic properties among different core@shell samples.

2.2.1. Synthesis of Small Au NPs. Au NPs were synthesized by the well-established citrate reduction method to be used as cores for the further formation of Au@Ag NPs [31,32]. Briefly, an aqueous solution of $HAuCl_4 \cdot 3H_2O$ (50 ml, 1.25×10^{-5} moles $HAuCl_4 \cdot 3H_2O$) is vigorously stirred and heated to reflux at 100 °C. Next, an aqueous solution of SC (0.5 ml, 0.17 moles SC) is added to the reaction solution. Refluxing is continued for 1 hour. The light yellow Au solution turns immediately clear and after 5 minutes the color changes to purple, slowly to dark purple and over time becomes a wine red colored solution. After refluxing, the mixture is cooled to room temperature and used without further processing. The Au NPs are a deep-red color with a LSPR band at 518 nm. Figure 4 shows the representative TEM and UV-Vis spectrum for the particles. The particles have a uniform and spherical morphology with a mean diameter of 14.2 ± 0.7 nm [20].

2.2.2. Synthesis of Large Au NPs. For the synthesis of relatively larger Au NPs, the general procedure followed is the same as above, but a much smaller ratio of SC is added [18]. An aqueous solution of $HAuCl_4 \cdot 3H_2O$ (50 mL, 1.25×10^{-5} moles $HAuCl_4 \cdot 3H_2O$) was vigorously stirred and heated to reflux at 100 °C. Then, an aqueous solution of SC (0.5 mL, 1.7×10^{-11} moles SC) was added to the reaction solution. Refluxing was continued for 1 hour. The light yellow Au solution turned immediately clear and after 5 minutes the color changed to purple, slowly to dark purple and over time became a light red/pink colored solution. After the refluxing, the mixture was cooled to room temperature and used for experiments without further processing. Figure 5 shows the TEM and UV-Vis spectrum collected for the Au NPs, illustrating the general morphology and optical properties. In general the particles have a spherical morphology with a

particle size distribution of 43.1 ± 4.3 nm. The SPR maximum occurs at 525 nm, consistent for Au NPs [18].

2.3 Synthesis of Ag@Au NPs

The effort to achieve the ideal Ag@Au NP structure has been highly elusive. Many studies have probed synthetic techniques including both organic and aqueous solvent based wet chemical methods, with mixed results. The galvanic replacement reaction causes a competition in the reduction of Au with the oxidation of the Ag core during typical deposition procedures. Careful control of the synthetic parameters in these reactions has led to the creation of quasi Ag@Au NPs with non-uniform structures such as NPs with partially hollow interiors, limited alloy formation, or non-continuous Au shells [5,9,10]. Sometimes the galvanic replacement reaction has been taken advantage of to create hollow Au structures templated from the original Ag NP core [6,7].

2.3.1. Synthesis of Acrylate Capped Ag@Au NPs. The acrylate capped Ag@Au NPs were synthesized as a platform to study the resulting plasmonic and structural properties for this class of nanomaterial [5]. Briefly, 50 ml of the dialyzed acrylate capped Ag particles (7.28×10^{-11} M Ag NPs) are brought to reflux and 10 ml of a $HAuCl_4\cdot3H_2O$ solution (ranging from 6.25×10^{-7} to 3.13×10^{-6} moles according to the thickness of the Au shell desired) and 10 ml of a SA solution (from 5.10×10^{-5} to 2.55×10^{-4} moles) are added drop-wise simultaneously. The solution color changes depending on the amount of Au added. In general, as Au and SA is added to the Ag NPs, the color changes from yellow-amber to dark amber to grey to grey-purple and finally to purple. Table 1 lists the metallic feeding ratio, moles of Ag and Au used in each synthesis as well as the resulting NP size as determined by TEM and composition determined from EDS and XPS. The primary difference between the EDS and XPS techniques is that EDS could be used to determine the composition of several different particles individually, then an average was taken, while for XPS a relatively large beam area results in simultaneous analysis of many particles at the same time.

Figure 6 shows a series of TEM images of the synthesized Ag@Au NPs. The NPs synthesized with atomic feeding ratio of 5% Au reveals particles with a uniform spherical morphology. For the Ag@Au NPs synthesized with an atomic feeding ratio of 15% Au, the particles retain the spherical morphology, but now several particles are observed that appear to have a light spot on the particle surface. These lighter colored spots arise from the formation of an incomplete Au shell on the Ag particle surface, a gap or hole in the Au shell occurring as a result of the galvanic replacement reaction [6,7]. Figure 7 shows a collection of Ag@Au NPs synthesized with 15% feeding ratio Au exhibiting a hole in the Au shell. Increasing the feeding ratio to 25% Au leads to many particles with a light center and thick dark outside. Now the particles seem to have adopted roughly hexagonal or pentagonal shapes, likely reflecting the tendency of Ag nanocrystals to be oriented in the twinned structure, templating the growth of Au at the surface. It is important to note that while the NPs synthesized with 15% Au feeding ratio show gaps or holes in the Au shell, they are still core@shell NPs, albeit with structural imperfections. This core@shell nature can be readily observed in a TEM study where an intense electron beam was applied to a single particle, as shown in Figure 8. The core@shell morphology is observed through the rupture of the Au shell, and the bursting (boiling) of the Ag core contained inside. As the particle is irradiated with a progressively stronger electron beam, the Au shell starts to peel back from the hole in the particle surface. The formation of a diamond shape in the shell indicates splitting of the Au shell. Finally the Au shell ruptures completely, causing the Au shell to collapse to a smaller dark ring. In addition the light material surrounding the remains of the Au shell is the Ag metal that has melted under the intense beam and has seeped to the area surrounding the particle. Such an observation is an excellent visual diagnostic for assessing the core@shell structure.

UV-Vis spectra and photographs of the Ag@Au NPs are shown in Figure 9, with the parent Ag core NP data included for reference [5,14]. In general, the color changes from a pale yellow, to slightly amber-yellow, and finally to purplish, for 5, 15 and 25% feeding ratio of Au,

respectively. It is important to note that these samples were all stable for several months of storage at ambient conditions with no signs of precipitation or changes in the coloring of the solution, which is aided by the removal of the excess reactants after synthesis. The UV-Vis spectra reveal an evolution in the plasmonic properties for the NPs as the amount of Au is increased in each sample. In general, the SPR band is slightly dampened in intensity for a feeding ratio of 5% Au. For a feeding ratio of 15% Au, the peak is significantly dampened, the peak is shifted to higher frequency and a new peak around 600 nm has emerged arising from Au. Finally for a feeding ratio of 25% Au, the Ag component of the SPR is completely dampened and only a broad peak is observed from the Au component.

2.3.2. Synthesis of Citrate Capped Ag@Au NPs. The as-synthesized citrate-capped Ag NPs were used as core particles in the synthesis of relatively larger sized Ag@Au NPs [18]. Briefly, the Ag NP dispersion (50 mL) is brought to reflux with stirring, and then $HAuCl_4 \cdot 3H_2O$ (8.31×10^{-7} moles, 10 mL, 0.0831 mM) and SC (8.49×10^{-4} moles, 10 mL, 0.849 mM) are simultaneously added dropwise. The reaction solution is refluxed for 1 hour. The yellow colored solution turns slightly orange after the coating of Au onto the Ag core. After refluxing, the mixture is cooled to room temperature and used for further experiments. Figure 10 shows the TEM image and UV-Vis absorption spectra of the as-synthesized Ag@Au NPs. The LSPR peak wavelength occurs at 423 nm with a single non-symmetrical shape observed between that for Ag and Au (only slightly shifted from the orginal Ag peak position) indicating the coating of Au onto the Ag NPs. The TEM image shows that the NPs have a roughly spherical morphology (a minor fraction of nanorods forms in the Ag NP synthesis but the occurrence is too low to significantly impact the optical properties). In addition, slightly darker rings outside the lighter spherical centers are observed indicating the formation of a Au shell on the Ag NP surfaces [5]. The mean size and size distributions 43.9 ± 7.9 nm for Ag@Au NPs.

EDS mapping analysis was conducted to study the relative positions of Ag and Au within the individual Ag@Au NPs [18]. Figure 11 shows the high angle annular dark field (HAADF)

image and the elemental mapping images for Ag, Au and an overlay of both. In general the dark field image reveals NPs with a dense outer shell and a relatively less dense inner area. When comparing this image to the Au map it is shown that a majority of the Au exists at the periphery of the NPs, which is expected for the formation of an Au shell. However, the Ag map also shows several particles with relatively less Ag in some particle centers. This can be attributed to partial etching of the Ag cores as Au is added in the coating procedure. While some etching may take place, a majority of the Ag remains, with a coating of Au forming over it, as can be observed in the overlay map of Ag and Au showing many particles with a majority of Ag concentrated inside the NPs and a majority of the Au concentrated at the periphery (shell) of the NPs.

2.4 Synthesis of Au@Ag NPs

The as-synthesized citrate-capped Au NPs were used as core particles (seeds) in the preparation of Au@Ag core@shell NPs [15,20]. The Au NP dispersion (20 ml) was brought to reflux with stirring, and then 5 ml of a 20 mM solution of $AgNO_3$ (1.0×10^{-4} moles) and 5 ml of a 13.5 mM solution of SC (6.75×10^{-5} moles) were simultaneously added dropwise. The reaction solution was refluxed for 20 minutes and then left to cool to room temperature. As a major advantage of the seed-mediated synthesis, the Ag shell thickness of the resulting Au@Ag core@shell NPs can be finely controlled by varying the amount of $AgNO_3$ added to the reaction solution. The Ag shell thickness of Au@Ag core@shell NPs was controlled by adding different amounts (0.3, 0.7, 1.8, and 3.2 ml) of 20 mM $AgNO_3$. Figure 12 shows the TEM images collected for each sample, revealing the four different Ag shell thicknesses obtained, including 0.4±0.3, 1.0±0.6, 2.2±0.4 and 3.6±0.4 nm, which correspond very closely to the theoretical shell thickness (0.45, 1.09, 2.29, and 3.48 nm, respectively) calculated from the metallic feeding ratio. The Ag shell thickness is expressed in the subscript hereafter, e.g. $Au@Ag_x$; *x* denotes the Ag shell thickness. Table 2 lists the size parameters of the NPs. It is noteworthy to point out that the resultant Au@Ag NPs are highly mono-disperse in terms of size and shape in comparison to Ag NPs synthesized by

comparable reduction methods. The UV-Vis spectra of all Au@Ag core@shell NPs are shown in Figure 13. When *x* was increased, the LSPR band gradually became blue-shifted, with the LSPR peak of Ag eventually becoming dominant. Finally, the $Au@Ag_{3.6}$ NPs show a single LSPR peak at 390 nm, which stems from the plasmon resonance of the Ag shells. The appearance of a monomodal LSPR band corresponding to Ag indicates that the Au cores are uniformly covered by the Ag shell and the optical contribution from the Au cores is completely screened. The significant blue-shift of the LSPR peak appearing in the Ag shell of the Au@Ag core@shell NPs suggests a higher electron density in the Ag shells than that of pure Ag NPs due to an electron transfer from the Au core to the Ag shell [33].

To provide definitive characterization of the core@shell nature of the Au@Ag NPs, STEM-HAADF imaging and EDS elemental mapping were performed [20]. Figure 14 shows a STEM-HAADF image of a single $Au@Ag_{3.1}$ NP as well as the corresponding two dimensional maps for Au and Ag in the particle. The high degree of atomic number (Z) based contrast offered by the STEM-HAADF technique allows the relative position of Au and Ag in the NP to be directly observed. The Au core is observed as the bright central region of the particle while the Ag appears as a lighter uniform halo around the brighter core. In addition, the EDS mapping result shows the relative locations of Au and Ag within the particle. Mapping of the Au M region is shown in green while the Ag L region is shown in red. By overlapping the two maps it is observed that the Au is located in the center of the particle area (the core) while the Ag is found on the outside (the shell). The collective EDS mapping and STEM-HAADF results provide definitive evidence of the Au@Ag structure of the particles.

2.4.1. Effect of Charge Transfer in the Galvanic Replacement Reaction. The galvanic replacement reaction is driven by the difference in the electrochemical potential between the two metals, with one serving as the cathode and the other as the anode. Regarding the general preparation of Ag@Au NPs, the reduction potential of $AuCl_4^-/Au$ (0.99 V vs SHE) is more positive than that of AgCl/Ag (0.22 V vs SHE) [34]. Hence, Ag NPs serve as sacrificial templates

being oxidized by $HAuCl_4$ according to Equation (1). This reaction is initiated locally at a high-energy site (e.g., surface step, point defect, or hole in the capping layer) [35] rather than over the entire surface. In the case that Au@Ag NPs are used as cores, however, the Ag shells are expected to have a higher electron density than Ag NPs due to electron transfer from the Au core to the Ag shell. The electron rich Ag shell results in a negative oxidation state, $Ag^{\delta-}$, and thus, may lead to effectively suppress the galvanic replacement reaction. Xia and coworkers also claimed a similar result in which a higher potential was required to oxidize Ag atoms contained in a Ag-Au alloy [34]. It was also reported that when the molar ratio of Au to Ag is more than 0.17, the galvanic reaction was hindered, indicating that a higher Au content can protect Au-Ag alloy NPs against galvanic etching [36]. Very possibly, the addition of Au changes the Ag reduction potential and alters the oxidative relationship between Ag^0 and $AuCl_4^-$. With respect to core@shell NPs, Liz Marzán and coworkers have synthesized Au@Ag, Au@Ag@Au and finally Au@Ag@Au@Ag multishell NPs using a similar synthetic approach to the present scheme [21]. In their approach however, the deposited intermediate Ag shell thickness was much greater than our own (ca. 32 nm), which resulted in the formation of hollow structures with partial alloying when the Au shell was deposited. In our own study, the intermediate Ag shell thickness is limited to the range where the charge transfer phenomenon takes place, allowing the ability to create Au@Ag@Au NPs without significant alloying or defects in the structure.

$$3Ag(s) + HAuCl_4(aq) \rightarrow Au(s) + 3AgCl(s) + HCl(aq) \quad (1)$$

2.5 Synthesis of Au@Ag@Au Double Shell NPs

This section describes the synthesis of Au@Ag@Au double shell NPs. The results illustrate the ability to control the thickness of the second Au shell deposited as well as the unusually uniform resulting particle structure. The uniform particle morphologies arise as a result of the suppression

of galvanic replacement though electronic transfer in the Au-Ag system, which is more fully explained in the later sections.

2.5.1. Synthesis of $Au@Ag_{3.6}@Au_{0.11}$ NPs. For the synthesis of $(Au@Ag_{3.6})@Au_{0.11}$ double shell NPs, a 20 ml as-synthesized $Au@Ag_{3.6}$ core@shell NP dispersion is refluxed with stirring until boiling, and then $HAuCl_4 \cdot 3H_2O$ (0.1 ml, 15 mM and SC (5 ml, 13.5 mM) are simultaneously added dropwise. The reaction solution is refluxed for 10 minutes and then left to cool to room temperature. After being coated by the second Au shell (theoretical thickness 0.15 nm), the LSPR peak is slightly red−shifted by about 10 nm indicating the formation of a thin Au shell onto the Ag surface. In Figure 15A, a TEM image of $Au@Ag_{3.6}@Au_{0.11}$ double shell NPs is shown. The $Au@Ag_{3.6}@Au_{0.11}$ double shell NPs are more uniform in size and shape when compared to typical Ag@Au NPs [37]. Moreover, they have no observable gaps or defects in the particle structure. When comparing the optical properties of Ag, $Au@Ag_{3.6}$ and $Au@Ag_{3.6}@Au_{0.11}$ NPs as shown in the UV-Vis spectra in Figure 15B, it can be observed that the spectral shape as well as the peak maxima changes. When Ag is coated onto the Au NPs, the SPR band maxima shifts to lower wavenumbers than that for pure Ag NPs. The band also becomes broadened at higher wavenumber values. When these $Au@Ag_{3.6}$ NPs are further coated with the second Au shell, the peak again shifts towards higher wavenumbers and retains the broadened spectral shape.

To further confirm the formation of the Au second shell, STEM−HAADF imaging and EDS elemental mapping were carried out for the $Au@Ag_{3.6}@Au_{0.11}$ double shell NPs [15]. Figure 16 shows the STEM−HAADF image (high Z contrast) of the $Au@Ag_{3.6}@Au_{0.11}$ double shell NPs. Since the heavier Au atoms (atomic number, Z = 79) give rise to a brighter image than the lighter Ag atoms (Z = 47) in the dark field image, the Au core appears brighter than the Ag first shell. One can see a very bright eggshell−thin layer on the Ag first shell. The thickness of the thin layer is 0.11 nm, which agrees well with the theoretical value (0.15 nm) calculated based on the amount of Au precursor added. This indicates that a thin continuous Au second shell was

successfully formed on the $Au@Ag_{3.6}$ NPs. The EDS mapping result also clearly indicates that the resulting NPs have a $Au@Ag_{3.6}@Au_{0.11}$ double shell structure.

2.5.2. Synthesis of $Au@Ag_{3.9}@Au_{1.2}$ NPs. A thicker coating of Au onto a $Au@Ag_{3.9}$ NP surface was achieved by following the above procedure and adding $HAuCl_4 \cdot 3H_2O$ (0.625 ml, 15 mM) and SC (5 ml, 13.5 mM) simultaneously dropwise [15]. Figure 17 shows a representative TEM image for the as-synthesized NPs. The NPs retain a sperical morphology with a size of 23.0 ± 1.9 nm with an intermediate Ag layer of 3.9 nm thickness and 1.2 nm second shell thickness for Au.

The particles display a clearly defined structure, which is elucidated using STEM images and the EDS elemental maps shown in Figure 18. The STEM image clearly shows the higher density Au in the particle center, with a less dense intermedaite layer from Ag, coated by a final second more dense layer of Au. The elemental maps further support the structural analysis with the Au L map showing Au existing in the NP center and the periphery, while the Ag L map shows a majority of the Ag in the intermediate space between the Au core and second Au shell. The overlay of these maps displays the relative positions for each metal in the NPs. Table 2 lists the size parameters of the double shell NPs.

3. MIE MODELLING OF THE PLASMONIC PROPERTIES OF Ag@Au NPS

Heterostructured Ag@Au core@shell NPs have been highly sought because of the expected enhanced plasmonic and reactivity properties, however, even for samples that seem to have a uniform structure, the optical properties do not always behave predictably. Mie Theory is a useful tool that can serve to clarify the resulting expected optical properties for this class of NP, enhancing the understanding of the particle structure and plasmonic properties relationship [14]. An important factor that must be considered is the parameters used in the calculation, which can have a large impact in the modeled results. The calculations here are based on Mie Theory for nanosized metallic spheres placed in water (dielectric constant = 1.77). In the theory, the metallic

dielectric function $\varepsilon(\omega) = 1-\omega_p^2/\omega(\omega+i\gamma)$ for the sphere is incorporated, where ω_p is the plasmon frequency depending on the specific metal. This approach differs from other well established modeling efforts in that the dielectric constant of the materials is expressed by the Drude Model as opposed to calculated from bulk materials using Energy Electron Loss Spectroscopy (EELS) [33]. The Drude Model offers an alternate approximation of the dielectric constants for nanoscale particles and provides an alternate expression of the optical properties for Ag@Au NPs [14]. The results in this section elucidate the challenges associated with attaining the ideal Ag@Au NP structure and provides a foundation for seeking alternate ways to control the particle stability and electronic properties to attain core@shell NPs with more uniform structures.

3.1 Mie Study of the Acrylate Capped Ag@Au NP Optical Properties

Three different models were used in the Mie calculations to elucidate the fine structural properties of the NPs [14]. Scheme 1 shows the models used with Mie theory to study the optical properties of the acrylate coated Ag@Au NPs, the corresponding realistic structures associated with each ideal model are also shown. Three models were used to represent the particle structures. Model I represents a Ag core with a complete coating of Au at the surface that corresponds to a realistic structure with thin and potentially non-uniform thickness of Au shell. Model II represents a Ag core, surrounded by a void space (water medium) which is completely encapsulated by a Au shell, corresponding to a realistic structure with Ag core exposed to the outside environment (water) and incomplete Au shell. Finally Model III is for a void space encapsulated by a layer of Ag which is further encapsulated by a layer of Au. This model corresponds to a realistic structure of a Ag core only partially in contact with the Au shell and a void space existing inside the particle.

When model 1 is considered, a thin coating of Au on the Ag core, a single prominent peak is observed in the Mie Modeling that shifts in position as a function of the relative size of the Ag core and the thickness of the Au shell. Figure 19 shows a comparison between the Mie Modeled optical properties for the core@shell Model 1 structure and an alloy. Functionally

speaking, the Mie results cannot solely be used to distinguish between the alloy and core@shell structured NPs because the spectral features of both types of NP are identical. This supports the notion that for very small dimensions (i.e. the nanoscale) there is a blurring of the lines between "phase segregated" and "alloy". In this case, the relative Au shell is too thin to display the properties of bulk Au, resulting in plasmonic properties more akin to an alloy than for a phase-segregated structure.

When Model II and III are considered, the UV-Vis spectra are significantly changed. Figure 20 shows the two sets of UV-Vis spectra calculated using Mie theory with the model II and III structures for the Ag@Au NPs. The insets to the spectra illustrate the structure used for the calculation as well as the structural parameters used. Model II represents Ag@Au NPs with an Ag core separated from the Au shell by a void space. These spectra show two primary peaks, the feature in the range of ~400-500 nm is attributed to the Ag core while the one at ~650-900 nm is attributed to the Au shell. The weak shoulder peak ranging between ~200-350 nm is attributed to the SPR band arising from the inner surface of the Au shell. As the size of the isolated Ag particle at the center of the structure is increased, the spectral component from Ag becomes more predominant while the Au component decreases in intensity and shifts to higher wavelength. Model III represents Ag@Au NPs with a central void space, then a layer of Ag coated by a layer of Au. In this case, a single broad feature is observed in the range of ~500-700 nm with two low intensity peaks in the range of ~200-300 nm. These low intensity peaks arise from the Ag-Au interface and the inner surface of Ag, while the primary broad peak arises from the outer surface of Au. This primary peak shifts to higher wavelength and decreases in intensity as the void space is increased in size and the Au layer is decreased in thickness.

The variation in the spectral shape allows a diagnostic comparison between experimentally collected spectra for acrylate capped Ag@Au NPs and the Mie theory calculated spectra. By qualitatively matching the two types of spectra, the general structural quality of the as-synthesized NPs can be determined. Figure 21 shows the UV-Vis spectra for three different

compositions of acrylate capped Ag@Au NPs along with the closest matching UV-Vis spectrum calculated using Mie theory. The insets to Figure 21 show the idealized structure used and a corresponding TEM image for an individual Ag@Au NP exhibiting the realistic core@shell structure. For the Ag@Au NPs synthesized with atomic feeding ratio of 5% Au (Figure 21A), Model I with parameters of R_1=0.7 and R_2=1 shows the best fit, which reflects a very thin and perhaps non-continuous Au shell. For the Ag@Au NPs with atomic feeding ratio of 15% Au (Figure 21B), Model II with parameters of R_1=0.3, R_2=0.45, and R_3=1 provides the best fit (though the spectra do show significant deviation, it is the spectral features that the fitting is based on). This reflects the fact that some particles display gaps in the Au coating, exposing the inner Ag, causing two peaks to be observed in the UV-Vis spectrum. Finally for the Ag@Au NPs with atomic feeding ratio of 25% Au (Figure 21C), Model III with parameters of R_1=0.6, R_2=0.8, and R_3=1 shows the best fit. This reflects the action of Au etching away some of the Ag core leaving a void space within the particle, with Au eventually forming a continuous shell over the core area.

The results indicate that when Au is coated onto pure Ag NP cores, inherently irregular structures result. The degree of imperfections in the structure can vary considerably by changing the reaction conditions such as amount of Au precursor added, temperature of reaction or addition of excess reducing agent, however the imperfections such as gaps in the Au shell or hollow spaces in the NP interior could never be eliminated because the galvanic replacement reaction could not be completely suppressed. The results illustrate the challenge associated with forming structurally controllable Ag@Au NPs. While the optical properties of these probes are potentially interesting and useful, the inability to eliminate the structural imperfections precludes the particles from practical use because the optical properties are inherently non-controllable and the NP stability in the presence of chloride ion would be poor. In response, the study inspires a new route towards Au/Ag based NPs with controllable optical/reactivity properties.

4. ELECTRONIC PROPERTIES OF Au@Ag NPS

The challenges associated in achieving a structurally ideal Ag@Au NP system led to a search for new strategies in creating Ag and Au based NPs with unique and controllable optical properties [15]. While the Ag@Au structure is popularly considered the "best" candidate to display strong optical/plasmonic properties as well as high chemical stability and bio-molecular reactivity, other less studied structures should also be considered. In addition, understanding of the interaction between Ag and Au in the NP synthesis procedure is important for controlling the resulting particle composition, structure, morphology, etc. With this in mind, it is known that a charge compensation mechanism occurs in the Au-Ag alloy system that leads to a depletion of *d* electrons at the Au site accompanied by an increase in *d* electrons at the Ag site [24,38]. In addition, a study on the Ag-Pt system where Ag adatoms were vapor-deposited onto a Pt(111) surface were found to increase d electron populations [39]. In light of these results, the electronic and chemical properties of the Ag component in an inverted Au@Ag particle structure could be tuned by taking advantage of the charge compensation mechanism. By increasing the electron density within the Ag shell, a negative Ag oxidation state would be achieved which could suppress the galvanic replacement reaction at the Ag shell surface and increase stability against oxidation. In order to probe the theory, Au@Ag NPs were synthesized, which inherently do not experience the galvanic replacement reaction. The NPs were studied using XPS and XANES techniques to explore the electronic properties of the Au and Ag particle components. The key to probing the charge compensation mechanism is to limit the Ag shell thickness to a range where the interfacial phenomenon can be observed.

4.1 XPS Analysis of the Electronic Characteristics

The electronic charge transfer phenomenon was studied in the citrate capped Au@Ag and $Au@Ag_{3.6}@Au_{0.11}$ NPs first by using XPS [15]. Figure 22 shows the high resolution XPS core–level spectra of Ag, $Au@Ag_x$, and $Au@Ag_{3.6}@Au_{0.11}$ double shell NPs. The Ag 3d core

levels are split into $3d_{3/2}$ and $3d_{5/2}$ spin–orbit pairs. Taking a closer look at the asymmetrically broadened $3d_{5/2}$ component, the overlapping peaks can be deconvoluted by using two Gaussian functions corresponding to Ag^0 and Ag–Au alloy (or Ag oxide) components. In the case of pure Ag NPs, the $3d_{5/2}$ component could be deconvoluted into Ag^0 (peak at 368.26 eV) and Ag oxide (peak at 367.8 eV) as shown in Figure 22B. On the other hand, in the cases of Au@Ag_x NPs, the $3d_{5/2}$ component could be divided into Ag^0 (peak at 368.18±0.03 eV) and Ag–Au alloy (peak at 368.5±0.03 eV) (Figure 22B). Importantly, no Ag oxide peak exists in the Au@Ag_x NPs even though the Ag first shell is exposed to the outside. The Au 4f area was also plotted as shown in Figure 22C. In support of the electronic transfer phenomenon, all of the Au@Ag_x NPs also exhibit a positive shift in the Au 4f BE (ca. 0.1 eV) compared to that of pure Au NPs which can be visualized by the addition of the vertical line in the Au $4f_{7/2}$ area in Figure 22D.

The Ag^0 $3d_{5/2}$ peak energy is plotted as a function of x as shown in Figure 23. All Au@Ag_x NPs exhibit a negative shift in the Ag^0 $3d_{5/2}$ BE compared to that of pure Ag NPs (368.26 eV). Moreover, the Ag^0 $3d_{5/2}$ BE increases toward the value of pure Ag NPs with increasing x when $x \geq 1.0$ suggesting that the charge transfer is an interfacial phenomenon. Interestingly, the deposition of the second Au shell onto the Ag surface again causes the reduction of Ag^0 $3d_{5/2}$ BE indicating further electron transfer between the Au second shell and the Ag first shell.

The XPS analysis on Au@Ag_x and Au@$Ag_{3.6}$@$Au_{0.11}$ NPs clearly illustrates that the general electronic properties of the two metals are modified in the core@shell structure and gives a basis for enhanced resistance to oxidation of the Ag shell, or the ability to deposit a second shell of Au [15]. This enhancement in the properties arises from the idea that the Ag shell becomes electron rich, however to understand the phenomenon more deeply, the charge transfer mechanism should be more fully understood. In order to gain a more diagnostic assessment of the charge transfer mechanism, XANES analysis was used to study the Au@Ag type NPs, offering a more rigorous understanding of the electronic transfer phenomenon.

A more in depth study of the XPS spectral line shape revealed an asymmetric broadening to higher binding energy in the Ag3d peaks which is attributed to the screening of a core hole by metallic conduction electrons [40]. The peak tailing can be described by the Doniach-Sunjic line shape, providing a more accurate fitting of the spectral data than simple multiple Gaussian functions. The asymmetry of the spectral shape is dictated by the screening constant of the core holes by gapless metallic excitations. For the Au@Ag_x NPs, this asymmetry factor is dependent on the Ag shell thickness, being more pronounced for thin Ag layers, which reinforces the interfacial nature of the phenomenon [40].

4.2 XANES Analysis of the Electronic Structure

XANES has been increasingly used to study the electronic properties for a wide range of materials including NPs. The technique has been employed to study the relationship between oxidation state and catalytic activity in catalysts [41,42,43], redox behavior [44,45,46], and for following the formation mechanism of metal NPs [47,48,49]. In this section of the study on the electronic properties for heterostructured Au@Ag NPs, the L-edge XANES analysis provides critical information on the charge transfer effect. In particular, the Au@Ag and Au@Ag@Au NPs are revealed to possess a unique electronic configuration in the Au $L_{2,3}$-edge XANES spectra.

The citrate capped Au@Ag and Au@Ag@Au NPs were analyzed using the XANES technique [19]. Figure 24 shows the XANES spectra in the Au L_2- and L_3-edges for Au foil, Au NPs, Au@$Ag_{1.0}$ NPs and Au@$Ag_{3.9}$@$Au_{1.2}$ NPs. All spectra showed the same resonance patterns as that of Au metal. In particular, the Au foil and Au NPs showed almost identical XANES spectra both in L_2- and L_3-edges. A gradual increase of the threshold resonance at the shoulder peak occurs in the order Au NPs < Au@$Ag_{1.0}$ NPs < Au@$Ag_{3.9}$@$Au_{1.2}$ NPs in L_2- and L_3-edges. The increase in the WL area in the L_2- and L_3- edge XANES spectra can be attributed to the decrease in 5*d* occupancy [50].

To further investigate the unoccupied d states, all relevant parameters were derived and listed in Table 3. Although small differences were detected in the hole densities between Au NPs and Au foil, it is reasonable to assume that there is relatively no electronic difference between them because the Au NPs have a relatively large diameter (14.4 nm) which is too large to exhibit size-dependent effects [51,52,53,54]. The values of both $\Delta h_{3/2}$ and $\Delta h_{5/2}$ increased in the Au@Ag core-shell NPs when compared to the Au NPs. From $Au@Ag_{1.0}$ core-shell NPs to the $Au@Ag_{3.9}@Au_{1.2}$ double-shell NPs, a further increase in both $\Delta h_{3/2}$ and $\Delta h_{5/2}$ was observed. This trend is a clear indication that the electron transfer from Au to Ag takes place in the heterostructured NPs.

A visual representation of the change in both *d*-orbital vacancy ($\Delta h_{3/2} + \Delta h_{5/2}$) and energy shift of the Au $4f_{7/2}$ XPS peak is shown in Figure 25. In the cases of $Au@Ag_{1.0}$ and $Au@Ag_{3.9}@Au_{1.2}$ NPs, an increase in the total *d*-orbital vacancies and a positive energy shift in the $4f_{7/2}$ peak were clearly observed. Importantly, both of them increase with increasing Ag-Au interfacial area. On the other hand, it has been previously observed that a negative shift in the Ag 3*d* peak energy occurs for both $Au@Ag_{1.0}$ and the $Au@Ag_{3.9}@Au_{1.2}$ NPs when compared to bare Ag NPs [15]. The collective results of XANES for Au and XPS for Au and Ag clearly illustrated that a unique charge transfer from Au to Ag occurs through the formation of a Au@Ag core-shell structure, and which is enhanced by Au outer-shell formation. It is expected that the electronic and chemical properties of the Ag shell can be tuned by coupling the Ag shell to the Au core due to a charge transfer that increases electron density within the Ag shell yielding a negative Ag oxidation state which suppresses the oxidation of the Ag shell [15].

5. ASSESSMENT OF THE STABILITY OF NPs

In this section, the relative stability of the various NPs are studied when exposed to a range of electrolytes. The ability to elucidate the stability properties of these NPs is vitally important in terms of oxidation and aggregation because these play a large role in affecting the sensing

properties. For example, the detection of many biomolecules requires a salt concentration approaching that of biological levels, which typically induces aggregation of the NP sensing probes, or in the case of chloride containing electrolytes, oxidation of the Ag component of the particles. The relative stability of Ag@Au NPs is breifly appraised, followed by a more in-depth look at the stability for the Au@Ag type NPs.

5.1 Stability of Ag and Ag@Au NPs Exposed to NaCl

One of the main expected advantages of Ag@Au NPs is an enhanced chemical stability compared to Ag NPs. The chemical stability of Ag and Ag@Au NPs in the presence of NaCl was studied to illustrate the clear difference in particle stability between these two types of probe. Ag NPs were first exposed to three different types of chloride containing electrolytes to demonstrate the severe instability. Figure 26 shows the representative TEM images obtained after 24 hours for adding NaCl (Fig. 26A), $CaCl_2$ (Fig. 26B) and HCl (Fig. 26C). The Cl^-/NP concentration ratio is fixed at 2.1×10^6 for each sample to standardize the relative amount of Cl^- ions available to react with Ag in each system. Each sample experienced the oxidative etching effect as evidenced by the appearance of large aggregates, larger particle sizes and overall a loss of particle dispersity. In these cases, the Ag has been completely oxidized and converted to AgCl through the oxidative etching process.

The understanding of the well known oxidative etching phenomenon that is responsible for the instability of Ag NPs exposed to chloride ions and atmospheric oxygen can give insight into how to limit the effect. In general, the oxidative etching process consists of three steps. First, metallic Ag becomes oxidized in the presence of oxygen as illustrated in Equation 2 [33,55]. Next, the silver oxide reaches an equilibrium state with the surrounding aqueous medium creating silver and hydroxide ions as shown in Equation 3 [33,56]. Finally, the Cl^- ions in the system react with the Ag ions to form insoluble AgCl, shown in Equation 4 [57]. In this way, as long as there is a sufficient supply of oxygen and Cl^- ions, a sample of Ag can be completely oxidatively etched

away, leading to AgCl. For our Ag NP sample, this readily occurs in the presence of each Cl-containing electrolyte system, leading to complete destruction of the original Ag NPs, forming non-disperse AgCl.

$$2Ag^0 + \frac{1}{2}O_2 \rightarrow Ag_2O(s) \quad (2)$$

$$Ag_2O(s) + H_2O \leftrightarrow 2Ag^+ + 2OH^- \quad (3)$$

$$Ag^+ + Cl^- \rightarrow AgCl(s) \quad (4)$$

To illustrate how the core@shell particle structure may protect Ag containing NPs from the oxidative etching phenomenon, a separate study was conducted where where 50 μL of NaCl solution (4.8 mM) was added to 1 mL of NP dispersion, then TEM images were taken after 1 hour of reaction [18]. Figure 27 shows the TEM images of the Ag@Au NPs taken before and 1 hour after adding the NaCl. The Ag@Au NPs retain the original morphology, qualititatively indicating that the Ag@Au NPs exhibit a superior stability as compared to the monometallic Ag NPs, despite the fact that gaps or holes exist in the Au shell. While the core@shell particle structure in this case is imperfect, the charge transfer effect is still operable, working to protect the remaining particle structure.

5.2 Stability of Au@Ag NPs Exposed to Cl Containing Electrolytes

The relative stability of the $Au@Ag_{3.1}$ NP probes was tested more rigorously by exposing them to various electrolytes, including chloride containing salts and acid including NaCl, $CaCl_2$ and HCl [20]. Addressing the stability of this class of NP probe in the presence of such electrolytes is essentially important, because the detection of many bio-molecules typically requires a buffer solution which contains significant amount of chloride containing electrolyte/salt including NaCl, KCl, $CaCl_2$, $MgCl_2$, and HCl [58], for example DNA will not denature without the presence of biological levels of salt. In addition, the exposure of Ag to the ambient atmosphere as well as chloride anions (Cl^-) is well known to lead to oxidative dissolution of the Ag, destroying Ag

based particles. The formation and ultimate understanding of how to manipulate the particle stability, optical, and electronic properties is expected to lead to more ready accessibility of highly active and robust NP probes for practical bio-molecular sensing and diagnostics applications.

The stability of the Au@Ag NPs was examined by exposing the NPs to NaCl, $CaCl_2$ or HCl [20]. Figure 28 shows the TEM images acquired for Au@Ag NPs exposed to the three different electrolytes with a Cl^-/NP concentration ratio of 2.1×10^6. In each case it can be observed that the NPs maintained a spherical morphology. For NaCl the NPs remain well despersed while for $CaCl_2$ or HCl, the particles appear to be partly aggregated, oftentimes forming chainlike structures. While the particle morphology remained spherical, the mean particle size decreased for each sample. For NaCl, the NP size decreased to 18.8 ± 1.6 nm (a Ag shell thickness of 2.3 nm), $CaCl_2$ showed a size of 16.1 ± 1.2 nm (a Ag shell thickness of 1.0 nm) while for HCl the particle size is about 15.6 ± 0.6 nm (a Ag shell thickness of 0.7 nm). While a sufficient amount of chloride was used to completely convert all of the Ag in the samples to AgCl (an order of magnitude more Cl^- than Ag for a ratio of 2.1×10^6), a large amount of elemental Ag appears to remain at the particle surface. The fact that the Ag shell thickness could not be completely eliminated suggests that a critical Ag layer thickness exists where the electron transfer phenomenon inhibits all oxidative etching, despite the amount of Cl^- added. In the case for NaCl, the retained NP stability in terms of resistance to aggregation has implications to bio-molecular sensing, especially in cases where high amounts of salt are required, for example in DNA detection where hybridization only occurs at salt levels of at least 0.05 M [8].

While the TEM results indicate that the NPs retain the general morphology properties the structure cannot be directly observed. To elucidate how much Ag metal remains at the $Au@Ag_{3.1}$ particle surface after interaction with chloride containing electrolyte, STEM-HAADF and EDS elemental mapping were used. Figure 29 shows the STEM-HAADF image and the elemental mapping results for Au and Ag for the NPs exposed to NaCl. It can be observed in the STEM-

HAADF image that the Au core still exists at the center of the particle after exposure to NaCl and more significantly that the Ag shell is still observed as the less bright halo at the particle periphery. The elemental mapping shows that the Au is contained in the particle interior while the Ag remains at the particle surface. The results show that the Au@Ag NPs retain their structural and compositional integrity, even after exposure to relatively high levels of NaCl [20].

STEM-HAADF and EDS elemental mapping were also used used to study the Au@Ag NPs exposed to $CaCl_2$ [20]. Figure 30 shows the morphology, structure and composition results for the Au@Ag NPs exposed to $CaCl_2$. In the STEM-HAADF image, the Au particle cores retained their morphological integrity as evidenced by the observation of the brighter spheres in the image. Some Ag also remains as evidenced by the less bright material observed between the Au cores. The elemental mapping shows that the Au is still confined to the particle interior (the core) while the material between the particles is Ag. A small amount of Ag is also observed as a thin layer at the particle periphery exposed to the outside medium. The images suggest that the individual Au cores are fused together with the remaining Ag.

Finally, for the case of exposing the $Au@Ag_{3.1}$ NPs to HCl, the STEM-HAADF and EDS elemental mapping analysis reveal a similar structure/morphlogy to the $CaCl_2$ case [20]. Figure 31 shows the STEM-HAADF and elemental mapping images taken for the Au@Ag NPs exposed to HCl. In the STEM-HAADF image a chain of fused NPs is observed with the Au cores appearing as the brighter spheres and the remaining Ag appearing as the less bright material between the Au cores. Some smaller particles are also observed in this image indicating that some AgCl particles formed through the oxidative etching process. The elemental mapping images confirm that the Au remains in the particle center (the core) while the material between the fused particles is Ag, with a thin layer of Ag remaining on the outside of the particles exposed to the outside medium. Chlorine was not observed, but a faint blue color can be observed in the overlay image (Fig. 31D) in the area surrounding the NP chain which indicates the presence of a faint amount of adventitiously adsorbed oxygen (mapping of the oxygen K line).

In general, the Au@Ag NPs showed enhanced stability when exposed to each of the different types of Cl-containing electrolytes, mainly because the first step in the oxidative etching process (Equation 2) is suppressed due to the electron transfer from the Au core to the Ag shell leading to a negative oxidation state for Ag. For the case of NaCl, the NPs resisted both aggregation and oxidative etching. For $CaCl_2$ and HCl cases, the particles displayed aggregation due to the de-protection of Au@Ag NP surfaces owing to the different effects of cations, but still resisted oxidative etching of the Ag shell. It is important to note that in all cases the Ag shell thickness was reduced after exposure to the different electrolytes, but a crital shell thickness exists where further etching appears to be suppressed, supporting the fact that the electron transfer effect is an interfacial phenomenon.

5.3 Stability of $Au@Ag_{3.6}@Au_{0.11}$ Double Shell NPs

The stability of $Au@Ag_{3.6}@Au_{0.11}$ double shell NPs was assessed in the presence of NaCl (0.5 M). In this case, the morphology was completely preserved (Figure 32) as a result of both the more negative Ag oxidation state and the fact that the Au second shell effectively protects the Ag first shell from contact with Cl^- ions. This suggests that the chemical stability of the $Au@Ag_{3.6}@Au_{0.11}$ NPs is extremely high even under severe conditions. The mean size of $Au@Ag_{3.6}@Au_{0.11}$ NPs before exposure to NaCl was 21.9 ± 1.2 nm as compared to 21.7 ± 1.6 nm 3 hours after exposure to NaCl, indicating that these NPs are highly stable in the presence of even very high levels of salt [15].

6. ASSESSMENT OF THE MOLECULAR SENSING PROPERTIES

In this section, the basic sensing properties for the core@shell NP probes is discussed. The results provide a preliminary assessment of the general plasmonic sensing properties. These sensing properties are probed primarily using the Raman analysis technique to identify well known reporter molecules. While the NPs used in these studies have not been optimized in terms of

particle size, shape or structure for the analysis, they nevertheless illustrate the ability to manipulate the particle parameters to achieve enhanced Raman activity. Ag is often considered the best SERS substrate because it has the largest optical cross section for any metal [18,20]. However, Ag NPs are often disadvantageous for use as sensing probes because of the propensity for oxidation, leading to non-reproducible sensing results [18,20]. To illustrate the enhanced properties of the heterostructured NPs (i.e. Ag@Au and Au@Ag NPs), the results in this section include the Ag NP sensing properties for comparison to the heterostructured NP results.

6.1 Assembly of the NPs Using Raman Active Molecules

The analysis relies on the assembly of the various NPs using two kinds of Raman active molecular linker systems with different chemical properties [18]. For the first linker system, rhodamine 6G dye (R6G) is used, relying on electrostatic interactions in the adsorption of the molecule to the NP surface. The second linker system used is a thiol containing molecule, 3-amino-1,2,4-triazole-5-thiol (ATT), which adsorbs to the NP surface *via* the sulfur functionality. Figure 33 shows the structure of these two types of Raman active linker molecule. Both molecules lead to spontaneous assembly of the different NP systems, which can be manipulated by controlling the concentration of ionic electrolytes in the assembly solution. The resulting aggregates exhibit Raman activity which is used to assess the general sensing properties of the various NP probes.

6.2 Molecular Sensing Properties of Citrate Capped Ag@Au NPs

The citrate capped Ag@Au NP probes were assembled using either R6G or ATT molecules, then the assemblies were rinsed with pure water and were dropped onto an APTMS-coated glass substrate [18]. The deposited NP assemblies were dried in air overnight, then Raman measurements were conducted. Figures 34A and 34B show the Raman spectra of NP assemblies

using R6G and ATT, respectively. In the case of R6G, primary and secondary peaks were observed at 1650 and 1357 cm^{-1} (both of which correspond to the C-C stretching vibration of the benzene ring) with several other weak bands. In this case Ag NPs show the highest SERS intensity as compared to other NP probes. In the case of ATT, the SERS spectra showed an intense band at 1340 cm^{-1} along with weak bands occurring at 1080, 1257 and 1417 cm^{-1}.

The SERS activities of these samples were quantified for direct comparison by calculating the relative enhancement factor for both samples [18]. In the case of R6G, the enhancement factor for Ag NPs (4957) was approximately 4 times higher than that of Ag@Au NPs (1157). This result suggests that the Au shell attenuates the Raman enhancement effect of the Ag core. On the other hand, in the case of ATT, Ag and Ag@Au NPs show nearly equal enhancement factors. The calculated enhancement factors for Ag and Ag@Au NPs are 23.5 and 19.5, respectively. These results can be explained on the basis of the different chemical nature of the two reporter molecules and on the mechanism of interaction with the NP surfaces. In the R6G system, the screening of electrostatic repulsion is responsible for the aggregation. All NPs are capped by negatively-charged citrate ions, and thus, the interaction strength between NP surfaces and R6G are the same regardless of composition of the NPs. In the ATT system, however, the NP assembly occurs *via* metal-sulfur bonding on the surface of particles followed by the electrostatic interaction between the negatively-charged citrate ions on the NP surfaces and positively-charged amine groups in ATT molecules. Because the Au-S interaction is stronger than Ag-S interaction, the number of ATT molecules adsorbed on the surface of a single Ag@Au NP is expected to be larger than that on a Ag NP. In the calculation of enhancement factor, it is assumed that the surfaces of NPs are completely covered by ATT molecules regardless of the type of NP. In reality, however, the number of ATT molecules in the Ag@Au NP assembly would be much larger than that in the Ag NP assembly. That is, Ag NPs essentially have the highest Raman enhancement factor and Ag@Au NPs have a lower enhancement factor than Ag NPs likely due to the attenuation effect of the Au shell. Nevertheless, Ag@Au NPs exhibit nearly the same SERS

intensity as Ag NPs when the linker molecule contains a thiol group. The most common means of the conjugation of biorelevant molecules onto metal NP surfaces is the utilization of metal-sulfur bonding, which is one reason why Ag@Au NP probes are competitive with Ag NP probes in terms of sensitivity.

6.3 Molecular Sensing Properties of $Au@Ag_x$ and $Au@Ag_{3.6}@Au_{0.11}$ NPs

The enhanced electronic properties observed for the Au@Ag NP structure make them intriguing as plasmonic probes for molecular/biomolecular sensing applications. In this section a breif assessment of the plasmonic sensing properties for the Au@Ag NP probes is presented. The sensing properties of these NP probes was tested with an experiment where Ag and Au@Ag NPs (1 mL of each) were exposed to NaCl (a Cl^-/NP concentration ratio of 2.1×10^7) and ATT (0.005 mM total ATT concentration, a large excess) [18]. After 24 hours of exposure, the precipitated NPs were gently rinsed with pure water to remove excess reactants, and then were dropped onto an APTMS coated glass substrate. The samples were dried in ambient conditions and were analyzed using Raman spectroscopy. Five different sample areas were inspected for both Ag and Au@Ag NP samples. Figure 35 shows the resulting Raman spectra collected for each sample. For the Ag NPs, a single broad peak with varying intensity is observed centered at about 1345 cm^{-1} while for the Au@Ag NPs, three distint peaks with relatively uniform intensity are observed at about 1270, 1355 and 1420 cm^{-1}. The Raman spectra collected for the Au@Ag NPs is characteristic for ATT laying flat on a metal surface through bidentate bonding arising from the triazole ring vibrations [59,60]. Because of the tendency for Ag NPs to be oxidatively reduced towards AgCl, the band observed at about 1345 cm^{-1} for the Ag NP sample probably originates from ATT molecules weakly adsorbed onto AgCl surfaces having a perpendicular orientation. Despite this, if it is assumed that the bands observed at 1345 and 1355 cm^{-1} for Ag and Au@Ag NPs are characteristic for ATT, the standard deviation associated with the intensity at the maxima of the peaks in each sample can be assessed. For the Ag NP case the average intensity was found

to be 93 ± 38 counts/sec while for the Au@Ag NPs the intensity is 207 ± 20 counts/sec. The Ag NPs show an intensity deviation of about 41% while the Au@Ag NPs have a deviation of only 10%. The experimental results show that the Au@Ag NPs display a reliable and reproducible sensing capability in the presence of salt and demonstrates the feasibility of using these materials in applications such as biomolecular detection that demand the presence of a high amount of electrolytes such as NaCl.

The Raman activity of the Au@Ag and $Au@Ag_{3.6}@Au_{0.11}$ NPs was further investigated using ATT [18,20]. It was found that the SERS activity dramatically increases with increasing *x* in the case of the $Au@Ag_x$ NPs [20]. Figure 36 shows the increasing Raman activity of the $Au@Ag_x$ NPs as well as the comparatively high activity of the $Au@Ag_{3.6}@Au_{0.11}$ NPs. The results illustrate the effect of increasing the Ag content in the particles which possess a high extinction coefficient and extremely high field enhancement. Moreover, the $Au@Ag_{3.6}@Au_{0.11}$ NPs exhibited a SERS activity as high as that for $Au@Ag_{3.6}$ NPs, indicating that the Au shell is operable in creating a strong reaction with the reporter molecule through the thiol functionality.

7. FUTURE OUTLOOK

The realization that heterostructuring in multicomponent NP systems offers an effective route for more closely controlling the resulting enhanced properties has led to a surge in interest in these materials. The ability to understand and manipulate the nanoscale phenomena through the NP structure will be an important advancement in integrating nanotechnology to the mainstream. In particular, the observation of the electronic transfer phenomenon in Au/Ag core@shell NPs is an important step in enhancing our ability to manipulate the novel properties of NPs for other important applications. The charge transfer effect has been demonstrated to be operable in the Au/Ag NP system, the plasmonic and stability properties of which can be greatly strengthened through careful manipulation of the NP structure, yet the true value of electronic transfer will be delineated in studies of other heterostructured systems. The phenomenon has the potential to

impact and lead to great advancements in the fields of catalysis, thermoelectrics, solar materials, magnetics and many other areas of high technology that stand to benefit from the incorporation of nanotechnology. As our understanding of how nanoscale phenomena operate, the drive to tailor or control the resulting NP properties will be a key necessity. The electronic transfer phenomenon will be one important tool for the future materials scientist in achieving that goal.

Acknowledgements

The authors would like to express their gratitude to Dr. Junya Ohyama (Nagoya Univ.) for advice with the XANES analysis. The synchrotron radiation experiments were performed at the BL01B1 station in the SPring-8 synchrotron radiation facility with the approval of the Japan Synchrotron Radiation Research Institute (JASRI) (proposal No. 2011A1607). We thank Dr. M. Koyano for his assistance in Raman measurement and K. Higashimine for assistance in the use of TEM and STEM instrumentation. This work was supported by the Japanese Grant-in-Aid for Scientific Research (C).

8. REFERENCES

1. (a) Mott D, Luo J, Smith A, Wang L Y, Njoki P N, Zhong C J, Nanoscale Research Letters, 2007; 2: 12. (b) Mott D, Luo J, Njoki P N, Lin Y, Wang L Y, Zhong C J, Catalysis Tod., 2007; 122: 378.
2. Cortie M B, McDonagh A M, Chem. Rev., 2011; 111: 3713.
3. Lauhon L J, Gudiksen M S, Wang D, Lieber C M, Nature, 2002; 420: 57.
4. Talapin D V, Nelson J H, Shevchenko E V, Aloni S, Sadtler B, Alivisatos A P, Nano Letters, 2007; 7: 2951.
5. Mott D, Nguyen T B T, Aoki Y, Maenosono S, Phil. Trans. R. Soc. A, 2010; 368: 4275.
6. Sun Y, Xia Y, Anal. Chem., 2002; 74: 5297.
7. Sun Y, Xia Y, J. Am. Chem. Soc., 2004; 126: 3892.

8. (a) Cao Y W, Jin R, Mirkin C A, J. Am. Chem. Soc., 2001; 123: 7961. (b) Rosi N L, Mirkin C A, Chem. Rev. 2005; 105: 1547. (c) Mirkin C A, Letsinger R L, Mucic R C, Storhoff J J, Nature, 1996; 382; 607. (d) Taton T A, Mirkin C A, Letsinger R L, Science, 2000; 289: 1757.

9. Cui Y, Ren B, Yao J L, Gu R A, Tian Z Q, J. Phys. Chem. B, 2006; 110: 4002.

10. (a) Šloufová I S, Vlčková B, Bastl Z, Hasslett T L, Langmuir, 2004; 20: 3407. (b) Šloufová I S, Lednicky F, Gemperle A, Gemperlova J, Langmuir, 2000; 16: 9928.

11. Yang Y, Shi J, Kawamura G, Nogami M, Scripta Mater., 2008; 58: 862.

12. Sun Y, Mayers B Y, Xia Y, Nano Lett., 2002; 2; 481.

13. Sun Y, Xia Y, Science, 2002; 298: 2176.

14. Mott D, Lee J D, Thuy N T B, Aoki Y, Singh P, Maenosono S, Japanese Journal of Applied Physics, 2011; 50: 065004-1.

15. Anh D T N, Singh P, Shankar C, Mott D, Maenosono S, Appl. Phys. Lett., 2011; 99: 073107.

16. Bi Y, Hu H, Lu G, Chem. Commun., 2010; 46: 598.

17. Pearson A, O'Mullane A P, Bansal V, Bhargava S K, Chem. Commun., 2010; 46: 731.

18. Singh P, Thuy N T B, Aoki Y, Mott D, Maenosono S, J. Appl. Phys., 2011; 109: 094301.

19. Nishimura S, Anh D T N, Mott D, Ebitani K, Maenosono S, J. Phys. Chem. C, 2012; 116 (7): 4511.

20. Shankar C, Anh D T N, Singh P, Higashimine K, Mott D M, Maenosono S, Nanotechnology, 2012; 23: 245704.

21. Lim I S, Ip W, Crew E, Njoki P N, Mott D, Zhong C J, Langmuir, 2007; 23: 826.

22. Mansour A N, Cook J W, Sayers D E, J. Phys. Chem., 1984; 88: 2330.

23. Mott N F, Proc. Phys. Soc. A, 1949; 62: 416.

24. Tyson C C, Bzowski A, Kristof P, Kuhn M, Sammynaiken R, Sham T K, Phys. Rev. B, 1992; 45: 8924.

25. Sham T K, Phys. Rev. B, 1985; 31: 1888.

26. Muller J E, Jepsen O, Wilkins J W, Solid State Commun., 1982; 42: 365.

27. Mattheiss L F, Dietz R E, Phys. Rev. B, 1980; 22: 1663.

28. Nemoshkalenko V V, Antonov V N, John W, Wonn H, Ziesche P, Phys. Stat. Sol. B, 1982; 111: 11.

29. Horsley J A, J. Chem. Phys., 1982; 76: 1451.

30. Smith N V, Wertheim G K, Hufner S, Traum M M, Phys. Rev. B, 1974; 10: 3197.

31. (a) Lim I S, Mott D, Ip W, Njoki P N, Pan Y, Zhou S, Zhong C J, Langmuir, 2008; 24: 8857. (b) Lim I S, Mott D, Engelhard M H, Pan Y, Kamodia S, Luo J, Njoki P N, Zhou S, Wang L, Zhong C J, Anal. Chem., 2009; 81: 689. (c) Lim I S, Goroleski F, Mott D, Kariuki N N, Ip W, Luo J, Zhong C J, J. Phys. Chem. B, 2006; 110: 6673.

32. Grabar K C, Freeman R G, Hommer M B, Natan M J, Anal. Chem., 1995; 67: 735.

33. (a) Mulvaney P, Linnert T, Henglein A, J. Phys. Chem., 1991; 95: 7843. (b) Henglein A, Chem. Mater., 1998; 10: 444. (c) Henglein A, Linnert T, Mulvaney P, Ber. Bunsen-Ges. Phys. Chem., 1990; 94: 1449.

34. Skrabalak S E, Chen J, Sun Y, Lu X, Au L, Cobley C M, Xia Y, Acc. Chem. Res., 2008; 41: 1587.

35. Wang Z L, J. Phys. Chem. B, 2000; 104: 1153.

36. Gong X, Yang Y, Huang S, J. Phys. Chem. C, 2010; 114: 18073.

37. Quian L, Yang X, Colloids Surf., A: 2005; 260: 79.

38. Roy R K, Mandal S K, Pal A K, Eur. Phys. J. B, 2003; 33: 109.

39. Rodriguez J A, Kuhn M, J. Phys. Chem., 1994; 98: 11251.

40. Maenosono S, Lee J D, Dao A T N, Mott D, Suf. Interface Anal., 2012, In Press.

41. Lytle F W, J. Catal., 1976; 43: 376

42. Tsuji A, Rao K T V, Nishimura S, Takagaki A, Ebitani K, ChemSusChem, 2011; 4: 542.

43. Ebitani K, Tanaka T, Hattori H, Appl. Catal. A: Gen., 1993; 102: 79.

44. Yamamoto T, Suzuki A, Nagai Y, Tanabe T, Dong F, Inada Y, Nomura M, Tada M, Iwasawa Y, Angew. Chem. Int. Ed., 2007; 46: 9253.

45. Nagai Y, Dohmae K, Teramura K, Tanaka T, Guilera G, Kato K, Nomura M, Shinjoh H, Matsumoto S, Catal. Today, 2009; 145: 279.

46. Shishido T, Asakura H, Amano F, Sone T, Yamazoe S, Kato K, Teramura K, Tanaka T, Catal. Lett., 2009; 131: 413.

47. Polte J, Ahner T T, Delissen F, Sokolov S, Emmerling F, Thunemann A F, Kraehnert R, J. Am. Chem. Soc., 2010; 132: 1296.

48. Abecassis B, Testard F, Kong Q, Francois B, Spalla O, Langmuir, 2010; 26: 13847.

49. Ohyama J, Teramura K, Higuchi Y, Shishido T, Hitomi Y, Kato K, Tanida H, Uruga R, Tanaka T, ChemPhysChem, 2011; 12: 127.

50. Qi B, Perez I, Ansari P H, Lu F, Croft M, Phys. Rev. B, 1987; 36: 2972.

51. Haruta M, Kobayashi T, Sano H, Yamada N, Chem. Lett., 1987; 405.

52. Tsunoyama H, Sakurai H, Negishi Y, Tsukuda T, J. Am. Chem. Soc., 2005; 127: 9374.

53. Comotti M, Pina C D, Matarrese R, Rossi M, Angew. Chem. Int. Ed., 2004; 43: 5812.

54. Jin R C, Nanoscale, 2010; 2: 343.

55. (a) Yin Y D, Li Z Y, Zhong Z Y, Gates B, Xia Y N, Venkateswaran S, J. Mater. Chem., 2002; 12: 522. (b) Blaser S A, Scheringer M, MacLeod M, Hungerbühler K, Sci. Total Environ., 2008; 390: 396. (c) Chen M, Wang L Y, Han J T, Zhang J Y, Li Z Y, Qian D J, J. Phys. Chem. B, 2006; 110: 11224. (d) Kumar R, Münstedt H, Biomaterials, 2005; 26: 2081.

56. Kapoor S, Langmuir, 1998, 14, 1021.

57. Shon Y S, Cutler E, Langmuir, 2004; 20: 6626.

58. (a) Polsky R, Gill R, Kaganovsky L, Willner I, Anal. Chem., 2006; 78: 2268. (b) Lee S., Cha E J, Park K, Lee S Y, Hong J K, Sun I C, Kim S Y, Choi K, Kwon I C, Kim K, Ahn C H, Angew. Chem., 2008; 120: 2846.

59. Wrzosek B, Bukowska J, J. Phys. Chem. C, 2007; 111: 17397.

60. Kudelski A, J. Phys. Chem. B, 2010; 114: 5180.

TABLES:

Table 1. Metallic Feeding Ratio, Moles of Ag and Au, TEM Determined Size and EDS/XPS Determined Compositions for Ag@Au NP samples. (Reproduced from reference 14).

Metallic Feeding Ratio	Moles Ag	Moles Au	TEM Size (nm)	EDS	XPS
$Ag_{95}Au_5$	1.25×10^{-5}	6.25×10^{-7}	17.5 ± 3.7	$Ag_{93.0}Au_{7.0}$	$Ag_{94.8}Au_{5.2}$
$Ag_{85}Au_{15}$	1.25×10^{-5}	1.88×10^{-6}	16.3 ± 2.7	$Ag_{60.6}Au_{39.4}$	$Ag_{57.7}Au_{42.3}$
$Ag_{75}Au_{25}$	1.25×10^{-5}	3.13×10^{-6}	17.5 ± 5.1	$Ag_{50.8}Au_{49.2}$	$Ag_{60.6}Au_{39.4}$

Table 2. Mean diameter and shell thicknesses of NPs. (Adapted from reference 15).

Type of NPs	*x* (nm)	*y* (nm)	*D* (nm)
Au	–	–	14.4 ± 0.7
$Au@Ag_{0.4}$	0.4 ± 0.3	–	15.2 ± 0.7
$Au@Ag_{1.0}$	1.0 ± 0.6	–	16.4 ± 1.2
$Au@Ag_{2.2}$	2.2 ± 0.4	–	18.8 ± 0.8
$Au@Ag_{3.1}$	3.1 ± 0.4	–	20.6 ± 1.2
$Au@Ag_{3.6}$	3.6 ± 0.4	–	21.6 ± 0.9
$Au@Ag_{3.6}@Au_{0.11}$	3.6 ± 0.4	0.11	21.8 ± 1.2
$Au@Ag_{3.9}@Au_{1.2}$	3.9 ± 0.7	1.2	23.0 ± 1.9

x: Ag first shell thickness, *y*: Au second shell thickness

Table 3. Derived parameters for the unoccupied *d* states. (Reproduced from reference 19).

Samples	ΔA_2 ($eV\cdot cm^{-1}$)	ΔA_3 ($eV\cdot cm^{-1}$)	$\Delta h_{3/2}$	$h_{3/2}$	$\Delta h_{5/2}$	$h_{5/2}$	$\Delta h_{3/2}+\Delta h_{5/2}$
Au foil*	0	0	0	0.118	0	0.283	0
Au NPs	157.1	–148.5	6.3×10^{-3}	0.124	-5.5×10^{-3}	0.278	7.8×10^{-4}
$Au@Ag_{1.0}$ NPs	383.0	617.2	1.5×10^{-2}	0.133	1.6×10^{-2}	0.299	3.1×10^{-2}
$Au@Ag_{3.9}@Au_{1.2}$ NPs	516.0	1340.6	2.1×10^{-2}	0.139	3.7×10^{-2}	0.320	5.7×10^{-2}

*Data from Ref. 27.

FIGURE CAPTIONS:

Scheme 1. The Mie Theory Modeled and Realistic Ag@Au Structures. (Reproduced from reference 14, Copyright 2011 Japan Society of Applied Physics).

Figure 1. (A) Schematic illustration of the Au $L_{2,3}$-edge XANES spectra and the corresponding electronic transitions. (B) Au $L_{2,3}$-edge XANES spectra and the difference spectrum in the case of Au foil. (Reproduced from reference 19, Copyright 2012 the American Chemical Society).

Figure 2. TEM (A) and UV-Vis spectrum (B) of as-synthesized Ag NPs capped with acrylate. (Adapted from reference 5).

Figure 3. TEM (A) and UV-Vis spectrum (B) of larger sized as-synthesized Ag NPs capped with citrate. (Adapted from reference 18, Copyright 2011 American Institute of Physics).

Figure 4. TEM (A) and UV-Vis spectrum (B) of as-synthesized smaller sized Au NPs capped with citrate. (Adapted from reference 20, Copyright 2012 IOP Publishing).

Figure 5. TEM image (A) and UV-Vis spectrum (B) of as-synthesized larger sized Au NPs capped with citrate. (Adapted from reference 18, Copyright 2011 American Institute of Physics).

Figure 6. TEM images of Ag@Au NPs with atomic feeding ratio of: 5% Au (A), 15% Au (B), and 25% Au (C). (Reproduced from reference 5).

Figure 7. Additional TEM images for Ag@Au NPs synthesized with an atomic feeding ratio of 15% Au showing NPs with gaps or holes in the Au shell of the nanostructures (indicated with arrows).

Figure 8. TEM electron beam radiation study for a single Ag@Au NP synthesized with atomic feeding ratio of 15% Au revealing the core@shell structure. (Reproduced from reference 5).

Figure 9. UV-Vis spectra for Ag and Ag@Au NPs prepared with increasing Au content, as-synthesized Ag NPs (black spectrum), 5% Au atomic feeding ratio (red), 15% Au atomic feeding ratio (blue) and 25% Au atomic feeding ratio (green). The inset shows photographs of the Ag and Ag@Au NPs with increasing shell thickness from left to right. (Adapted from reference 14, Copyright 2011 Japan Society of Applied Physics).

Figure 10. TEM image (A) and UV-Vis spectrum (B) of as-synthesized Ag@Au NPs capped in citrate with relatively larger size. (Adapted from reference 18, Copyright 2011 American Institute of Physics).

Figure 11. STEM-HAADF (A) and EDS elemental mapping images of citrate capped Ag@Au NPs for Au M map (B), Ag L map (C) and an overlay of the Au and Ag maps (D). The scale bar in (A) applies to all images. (Adapted from reference 18, Copyright 2011 American Institute of Physics).

Figure 12. TEM images for Au@Ag NPs synthesized with increasing Ag shell thickness: 0.4 (A), 1.0 (B), 2.2 (C), 3.1 (D) and 3.6 (E) nm. (Adapted from reference 15 and 20, Copyright 2011 American Institute of Physics and 2012 IOP Publishing).

Figure 13. UV-Vis spectra for as-synthesized Au@Ag NPs with varying Ag shell thickness, the arrows represent the dampening of the Au SPR band with a concurrent increase in the SPR band intensity for Ag as the Ag shell thickness is increased. The inset to the figure shows a photograph of the Au, and Au@Ag_x NPs with Ag shell thicknesses of 0.4, 1.0, 2.2, and 3.6 nm, from left to right. The data for Au NPs is included for comparison. (Adapted from reference 15 and 20, Copyright 2011 American Institute of Physics and 2012 IOP Publishing).

Figure 14. STEM-HAADF (A) and EDS elemental mapping images of Au@Ag NPs for Au M map (B), Ag L map (C) and an overlay of the Au and Ag maps (D). The scale bar in (A) applies to all images. (Reproduced from reference 20, Copyright 2012 IOP Publishing).

Figure 15. TEM image for $Au@Ag_{3.6}@Au_{0.11}$ NPs (A) and UV-Visible spectra (B) for Ag (black curve), $Au@Ag_{3.6}$ (red curve) and $Au@Ag_{3.6}@Au_{0.11}$ (blue curve). (Adapted from reference 15, Copyright 2011 American Institute of Physics).

Figure 16. STEM-HAADF (A) and EDS elemental mapping images of $Au@Ag_{3.6}@Au_{0.11}$ NPs for Au M map (B), Ag L map (C) and an overlay of the Au and Ag maps (D). The scale bar in (A) applies to all images. (Reproduced from reference 15, Copyright 2011 American Institute of Physics).

Figure 17. TEM image of $Au@Ag_{3.9}@Au_{1.2}$ NPs.

Figure 18. STEM-HAADF (A) and EDS elemental mapping images of $Au@Ag_{3.9}@Au_{1.2}$ NPs for Au L map (B), Ag L map (C) and an overlay of the Au and Ag maps (D). The scale bar in (A) applies to all images. (Reproduced from reference 15, Copyright 2011 American Institute of Physics).

Figure 19. UV-Visible spectra calculated using Mie theory for alloy AgAu NPs (A), and for Ag@Au NPs with the Model I structure (B). (Reproduced from reference 14, Copyright 2011 Japan Society of Applied Physics).

Figure 20. UV-Visible spectra calculated using Mie theory for Ag@Au NPs using Model II (A), and Model III (B). (Reproduced from reference 14, Copyright 2011 Japan Society of Applied Physics).

Figure 21. UV-Visible spectra for the three different types of Ag@Au NPs synthesized along with the corresponding best fit spectra calculated using Mie theory for atomic feeding ratio of 5% Au and Model I (A), atomic feeding ratio of 15% Au and Model II (B), and atomic feeding ratio of 25% Au and Model III (C), respectively. (Reproduced from reference 14, Copyright 2011 Japan Society of Applied Physics).

Figure 22. XPS spectra of Ag, $Au@Ag_x$ (x = 0.4, 1.0, 2.2 and 3.6), and $Au@Ag_{3.6}@Au_{0.11}$ double shell NPs in the Ag3d (A) area with an expanded view of the $Ag3d_{5/2}$ component (B). XPS spectra in the Au4f area are shown in (C) with an expanded view of the $Au4f_{7/2}$ area (D). The deconvolution shown for the $Ag3d_{5/2}$ area corresponds to Ag^0 (blue curves) and Ag@Au alloy (red curves) [or Ag oxide (red dashed curve)] components. The blue line in (D) aids in visualizing the subtle peak shift. (Adapted from reference 15, Copyright 2011 American Institute of Physics).

Figure 23. Plot of the $Ag3d_{5/2}$ Peak Energy for the $Au@Ag_x$ and $Au@Ag_{3.6}@Au_{0.11}$ double shell NPs. (Adapted from reference 15, Copyright 2011 American Institute of Physics).

Figure 24. (A) Au L_2-edge and (B) Au L_3-edge XANES spectra of Au foil, Au NPs, $Au@Ag_{1.0}$ NPs and $Au@Ag_{3.9}@Au_{1.2}$ NPs. The insets show an expanded view. (Adapted from reference 19, Copyright 2012 the American Chemical Society).

Figure 25. Differences of the *d*-orbital vacancies from bulk Au and XPS energy shift in the $4f_{7/2}$ peak from bulk Au.

Figure 26. TEM images for Ag NPs (A) exposed to NaCl (B), $CaCl_2$ (C) and HCl (D) after 24 hours when the Cl^-/NP concentration ratio is 2.1×10^6. (Adapted from reference 20, Copyright 2012 IOP Publishing).

Figure 27. TEM images of Ag@Au NPs before (A) and 1 hour after (B) adding NaCl. (Adapted from reference 18, Copyright 2011 American Institute of Physics).

Figure 28. TEM images of Au@Ag NPs for NaCl (A), $CaCl_2$ (B) and HCl (C) after 24 hours when the Cl^-/NP concentration ratio is 2.1×10^6. (Adapted from reference 20, Copyright 2012 IOP Publishing).

Figure 29. STEM-HAADF image (A), and EDS elemental mapping of Au@Ag NPs in NaCl after 24 h when the Cl^-/NP ratio is 2.1×10^6 for Au M map (B), Ag L map (C) and an overlay of the Au and Ag maps (D). The scale bar in (A) applies to all images. (Reproduced from reference 20, Copyright 2012 IOP Publishing).

Figure 30. STEM-HAADF image (A), and EDS elemental mapping images of Au@Ag NPs for $CaCl_2$. after 24 hours when the Cl^-/NP concentration ratio is 2.1×10^6 for Au M map (B), Ag L map (C) and an overlay of the Au and Ag maps (D). The scale bar in (A) applies to all images. (Reproduced from reference 20, Copyright 2012 IOP Publishing).

Figure 31. STEM-HAADF image (A), and EDS elemental mapping images of Au@Ag NPs for HCl after 24 hours when the Cl^-/NP concentration ratio is 2.1×10^6 for Au M map (B), Ag L map (C) and an overlay of the Au and Ag maps (D). The scale bar in (A) applies to all images. (Reproduced from reference 20, Copyright 2012 IOP Publishing).

Figure 32. TEM image of $Au@Ag_{3.6}@Au_{0.11}$ NPs 3 hours after adding NaCl. (Adapted from reference 15, Copyright 2011 American Institute of Physics).

Figure 33. Chemical structures of (a) R6G and (b) ATT.

Figure 34. Raman spectra of NP assemblies created by using (A) R6G and (B) ATT. Bottom, middle and top curves represent the spectra of Ag, Ag@Au and Au NP assemblies, respectively. The labelled peaks are used for calculation of enhancement factor. (Adapted from reference 18, Copyright 2011 American Institute of Physics).

Figure 35. Raman spectra taken for Ag NPs (A) and Au@Ag NPs (B) exposed to ATT and NaCl with a Cl^-/NP concentration ratio of 2.1×10^7. (Reproduced from reference 20, Copyright 2012 IOP Publishing).

Figure 36. Raman spectra of $Au@Ag_x$ (from bottom to top, x = 0.4, 1, 2.2, and 3.6 nm) and $Au@Ag_{3.6}@Au_{0.11}$ (top curve) NP assemblies created by using ATT. (Adapted from reference 15, Copyright 2011 American Institute of Physics).

FIGURES:

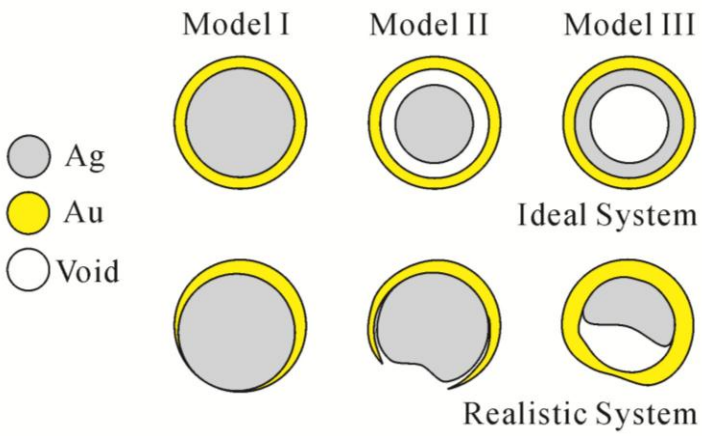

Scheme 1

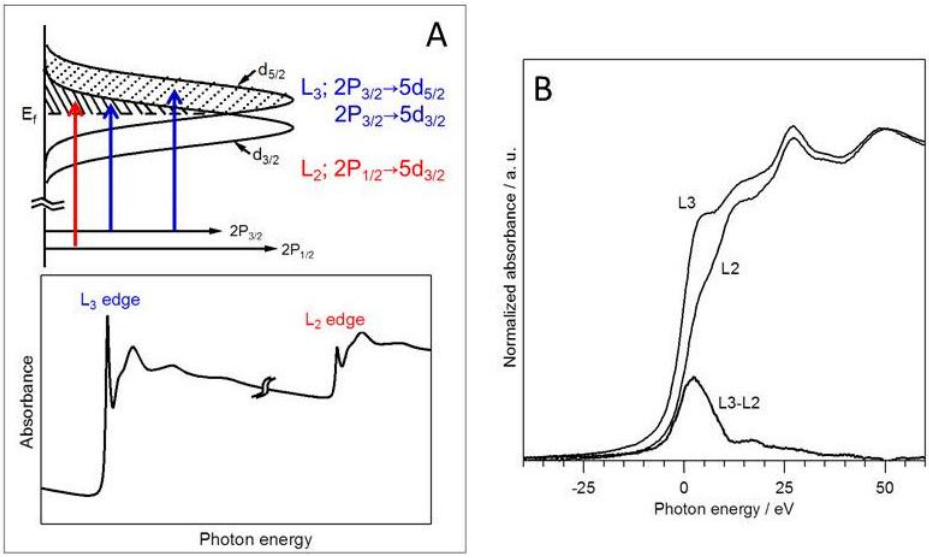

Figure 1

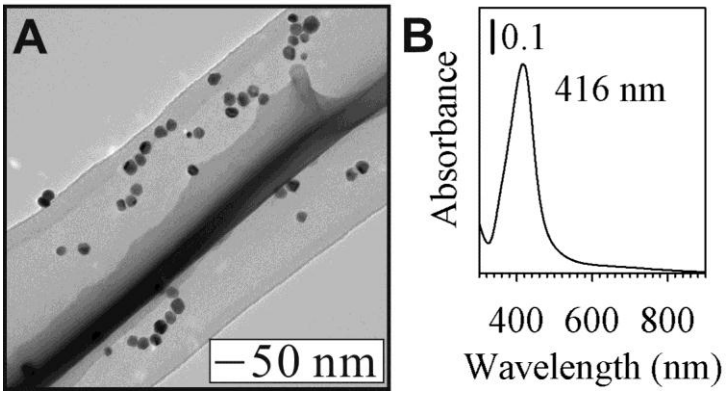

Figure 2

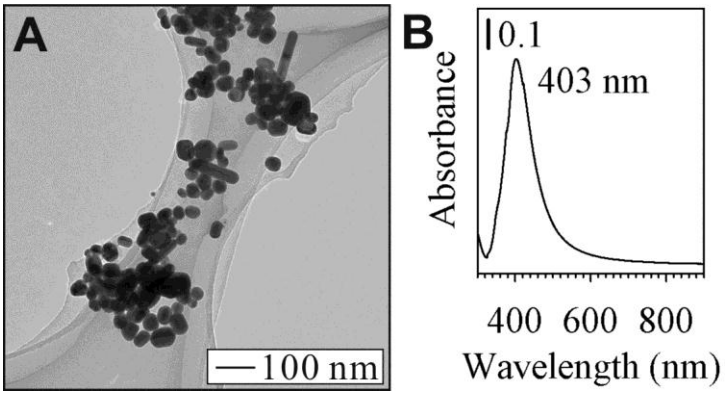

Figure 3

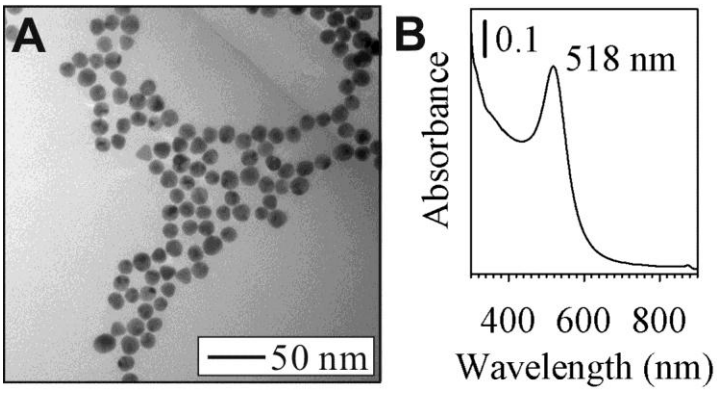

Figure 4

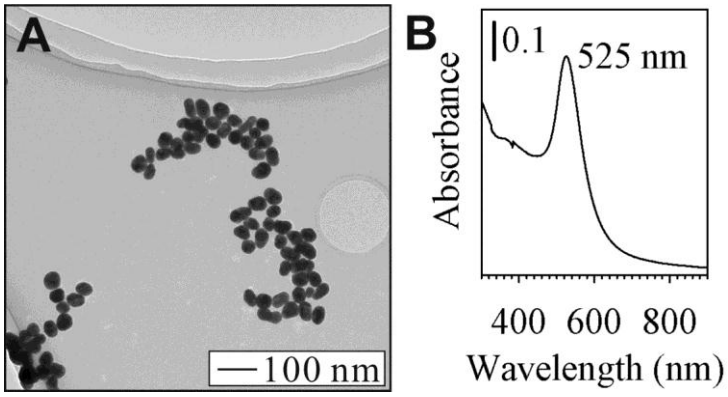

Figure 5

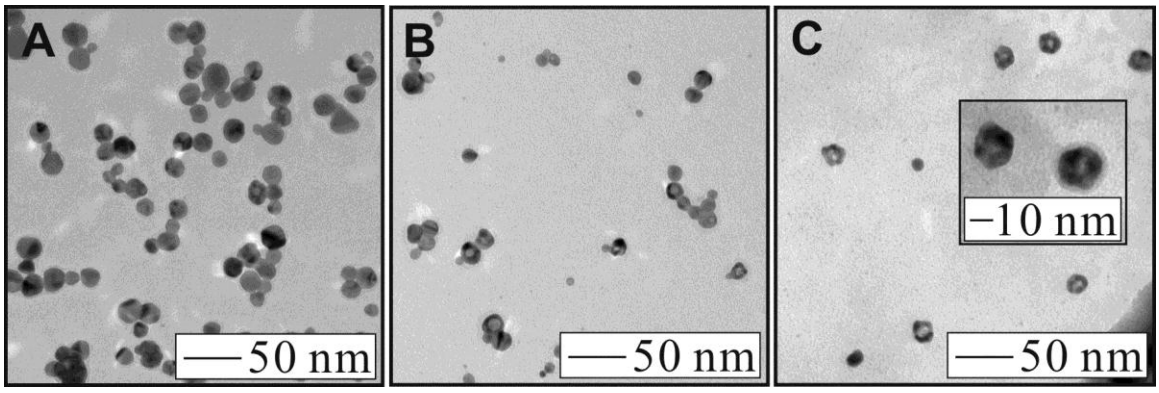

Figure 6

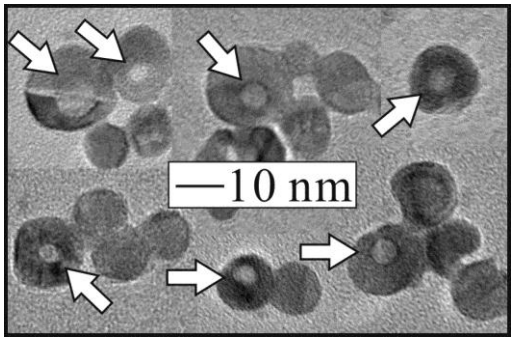

Figure 7

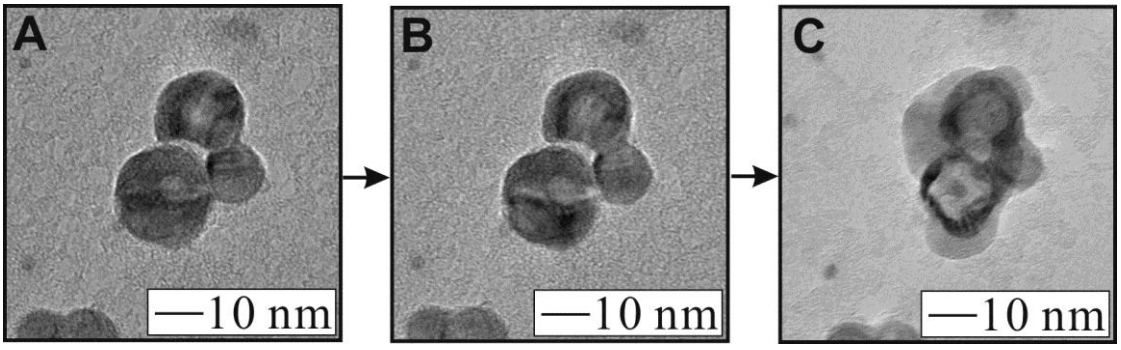

Figure 8

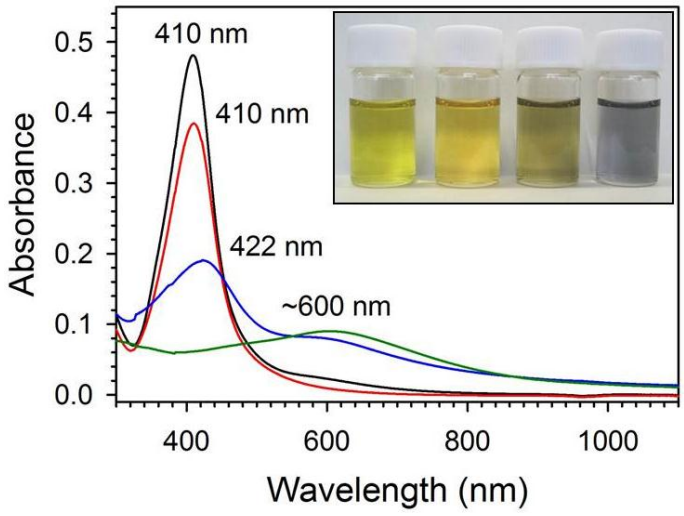

Figure 9

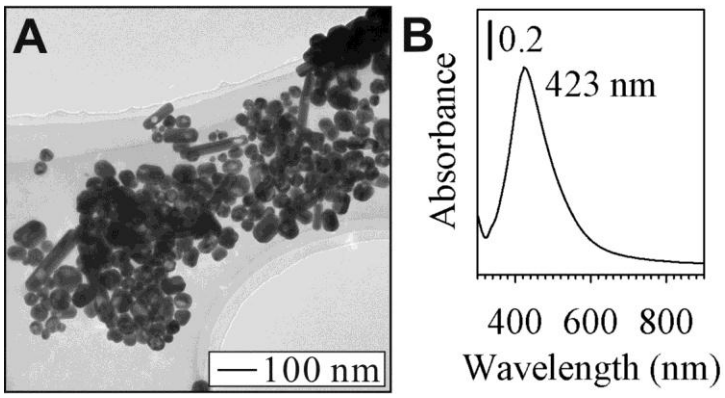

Figure 10

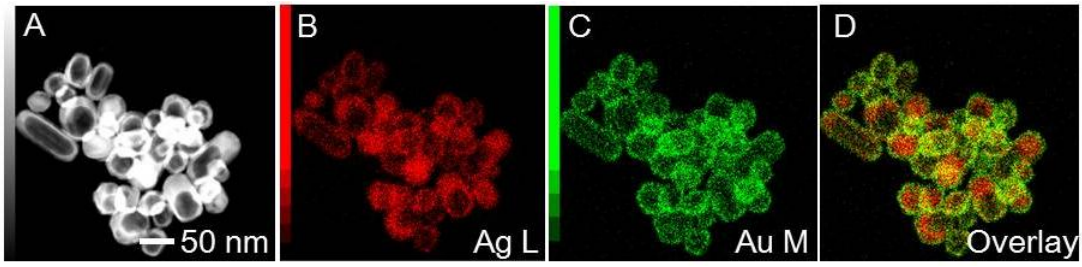

Figure 11

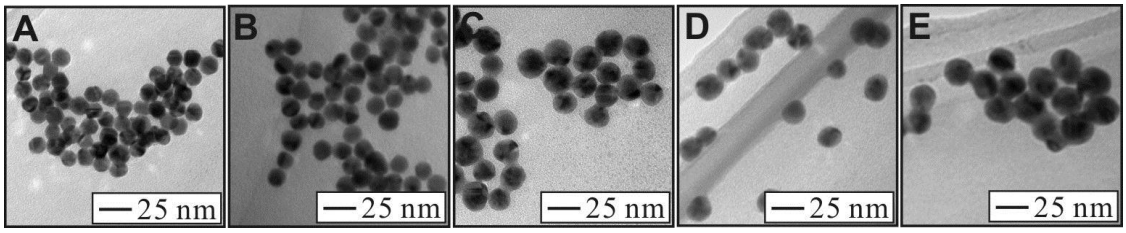

Figure 12

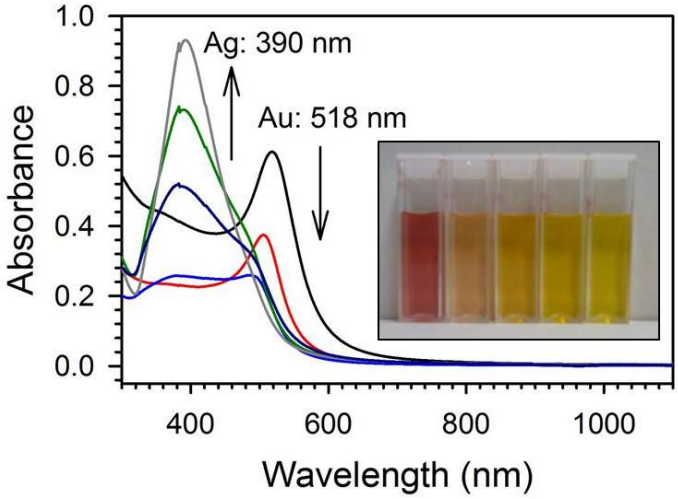

Figure 13

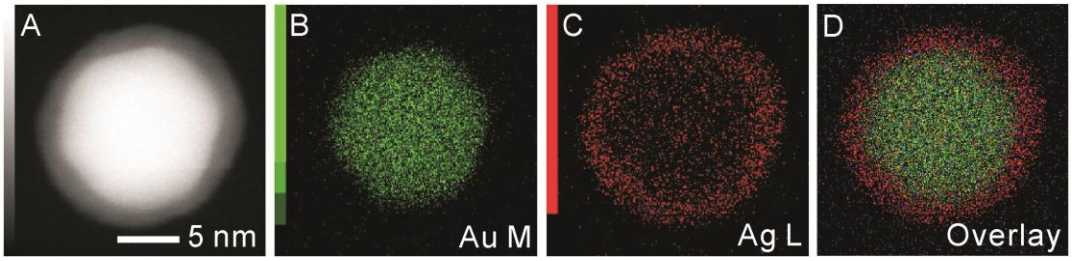

Figure 14

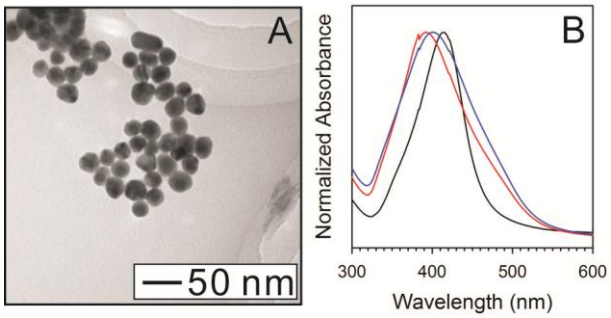

Figure 15

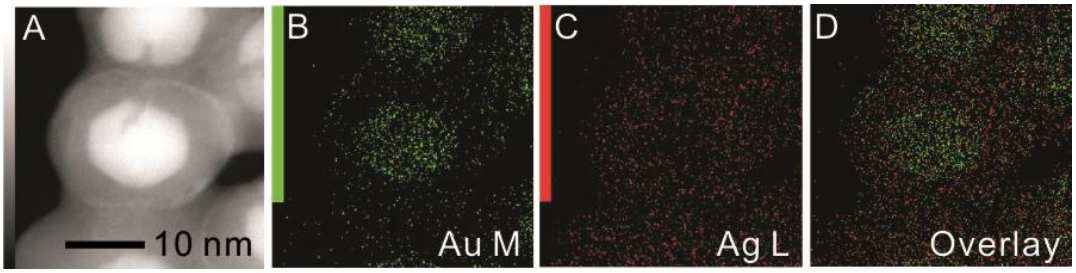

Figure 16

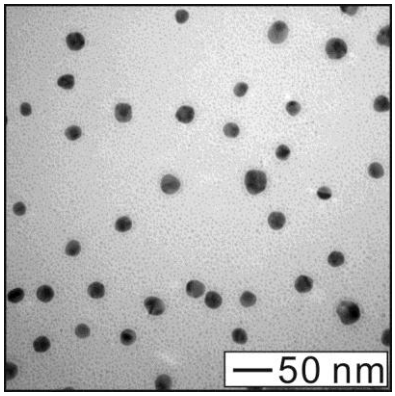

Figure 17

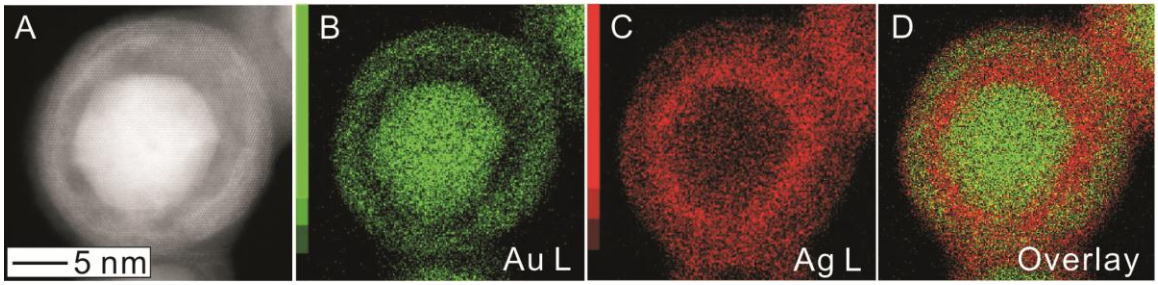

Figure 18

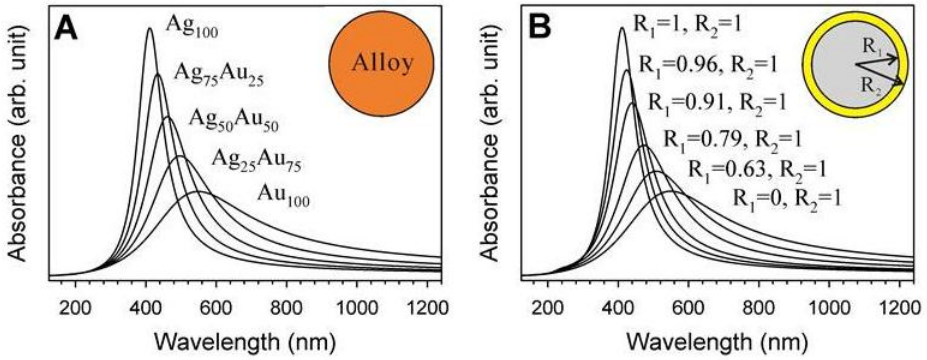

Figure 19

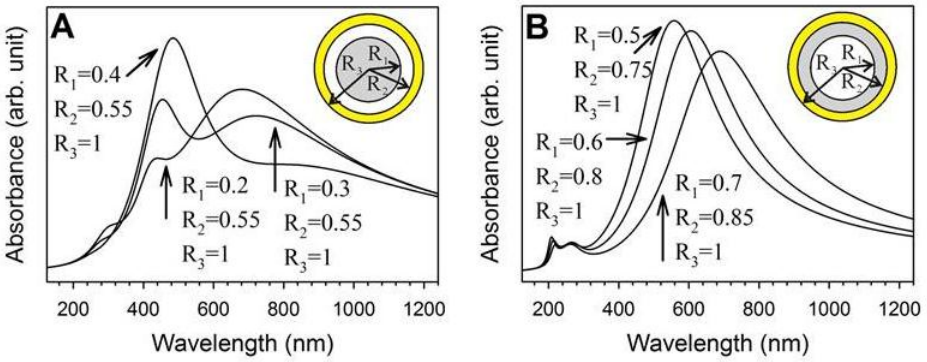

Figure 20

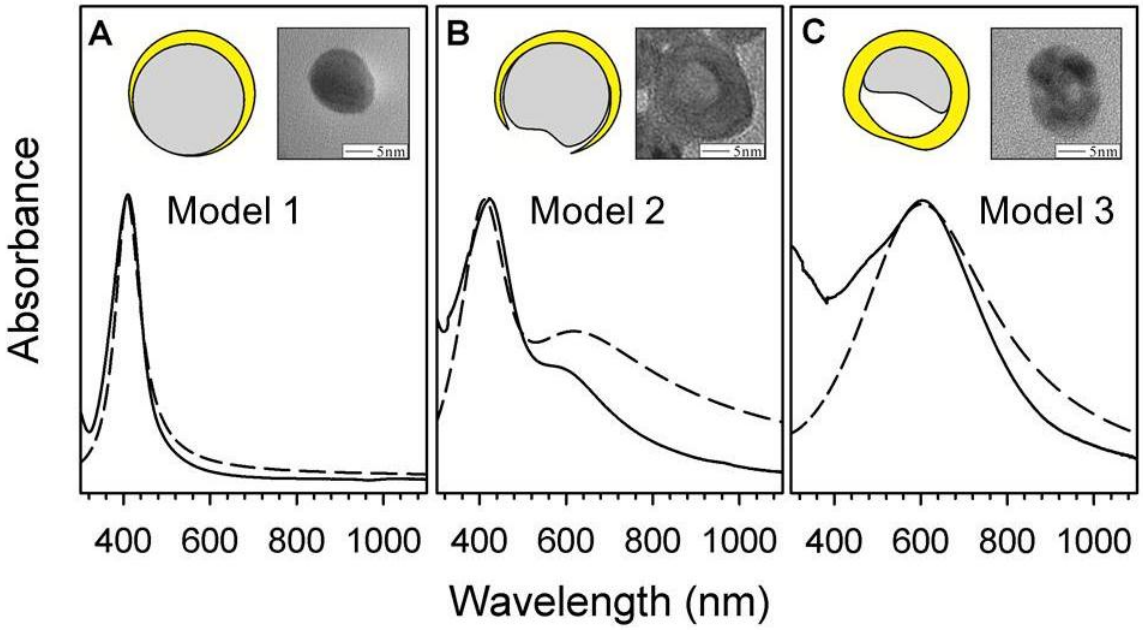
A
B
C
5nm
Model 1
Model 2
Model 3
Absorbance
400 600 800 1000
Wavelength (nm)

Figure 21

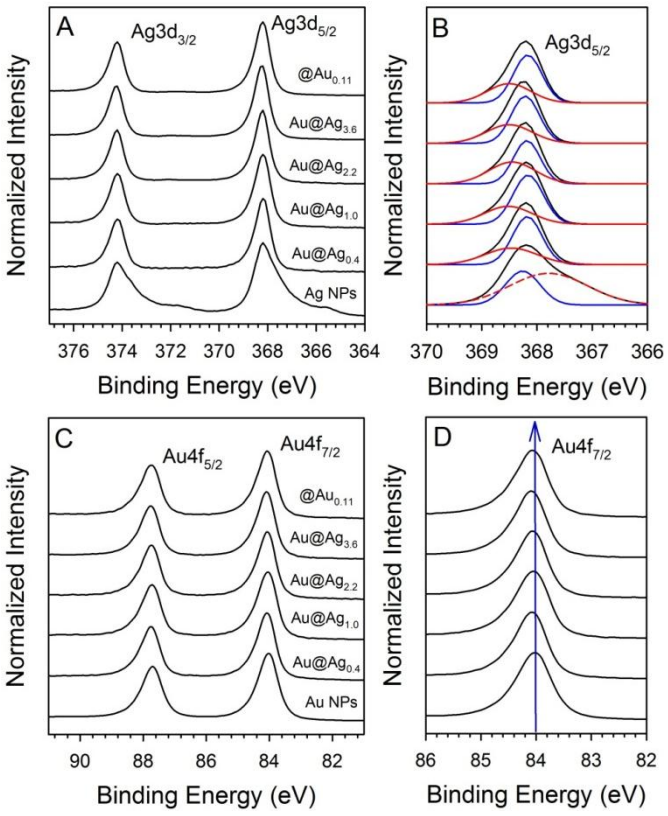
A
Ag3d3/2
Ag3d5/2
@Au0.11
Au@Ag3.6
Au@Ag2.2
Au@Ag1.0
Au@Ag0.4
Ag NPs
Normalized Intensity
376 374 372 370 368 366 364
Binding Energy (eV)
B
Ag3d5/2
370 369 368 367 366
C
Au4f5/2
Au4f7/2
Au NPs
90 88 86 84 82
D
86 85 84 83 82

Figure 22

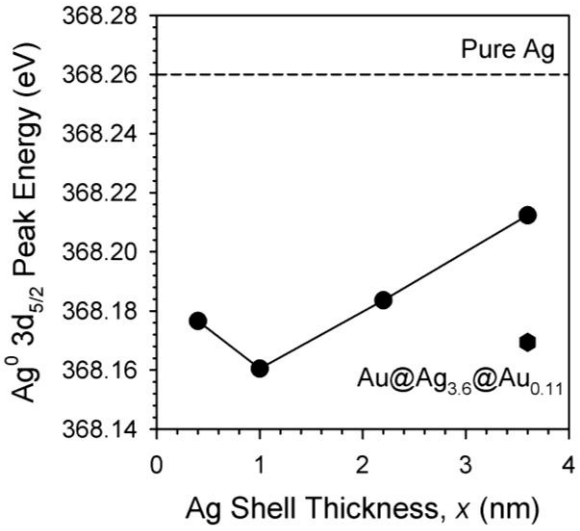

Figure 23

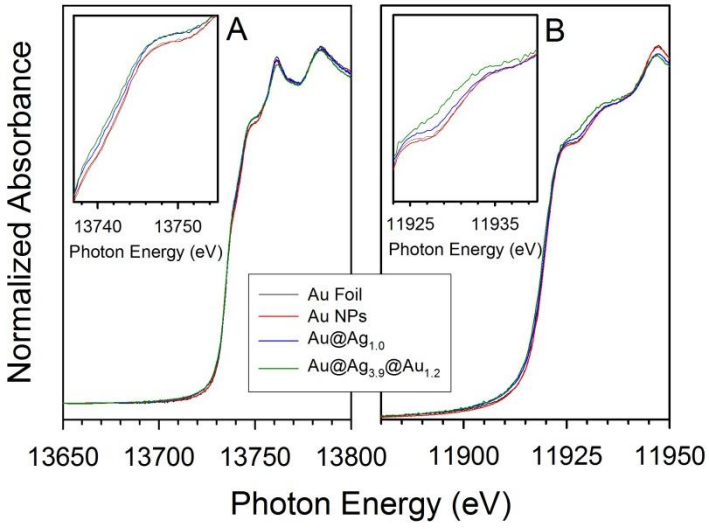

Figure 24

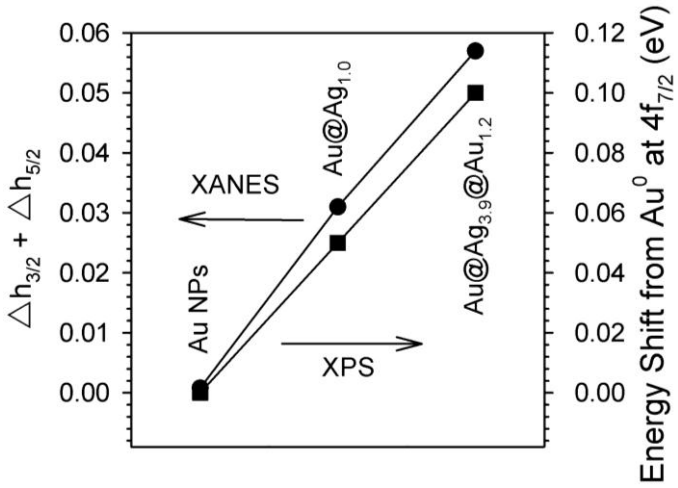

Figure 25.

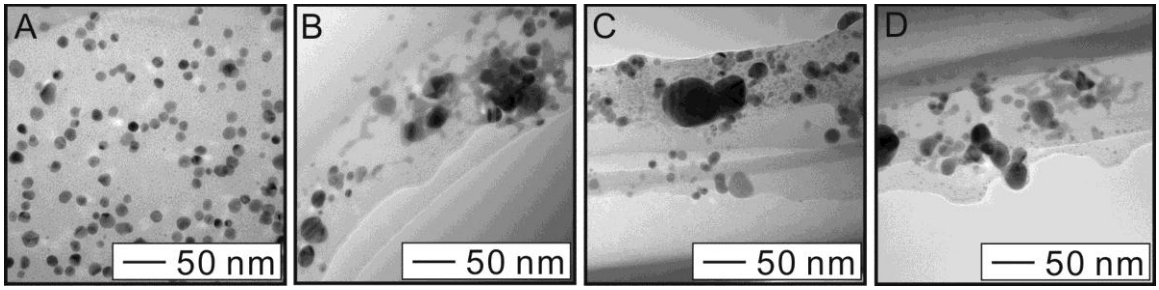

Figure 26

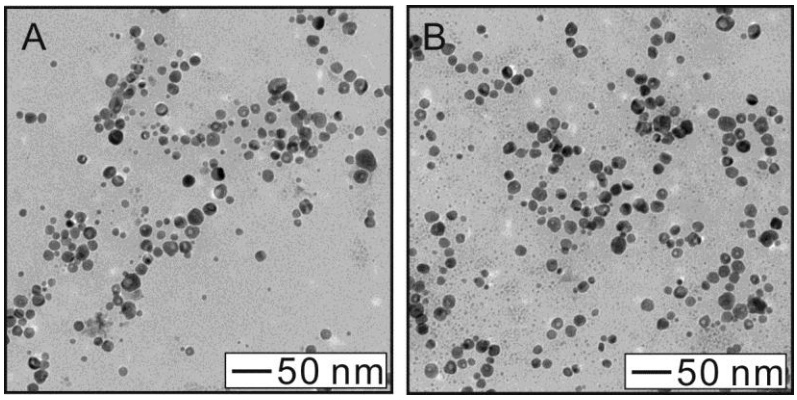

Figure 27

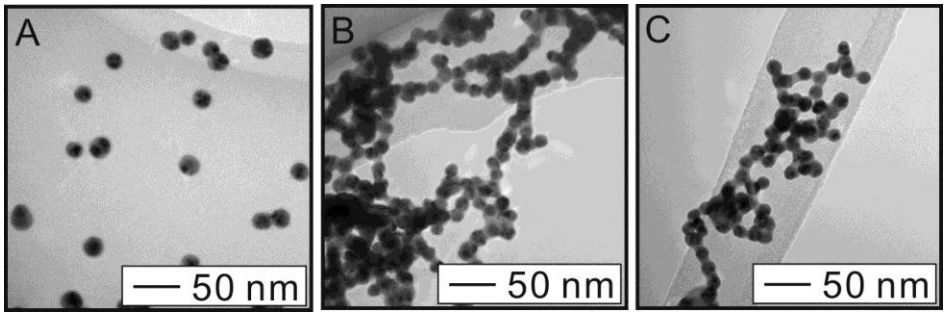

Figure 28

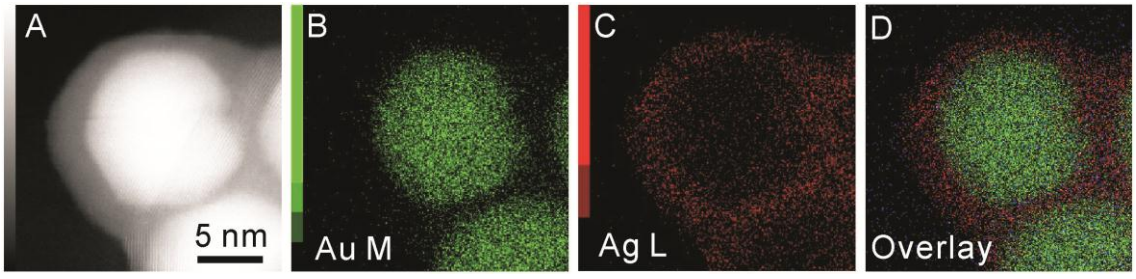

Figure 29

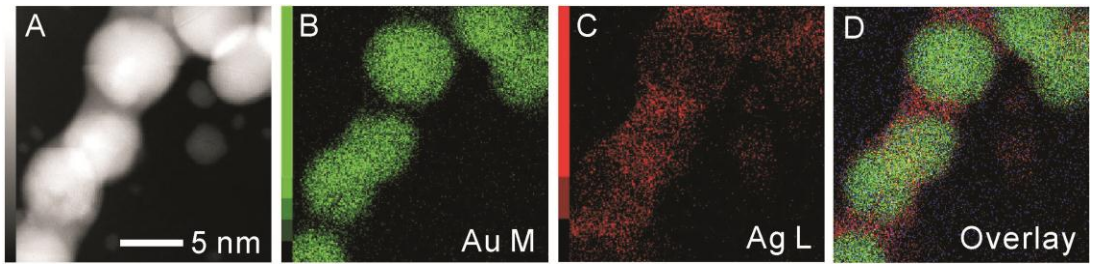

Figure 30

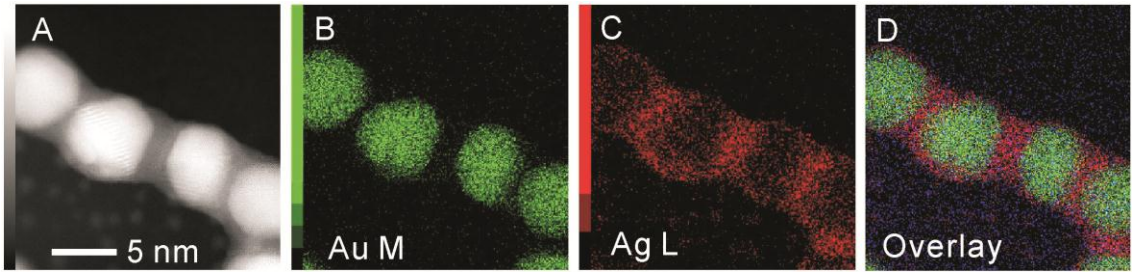

Figure 31

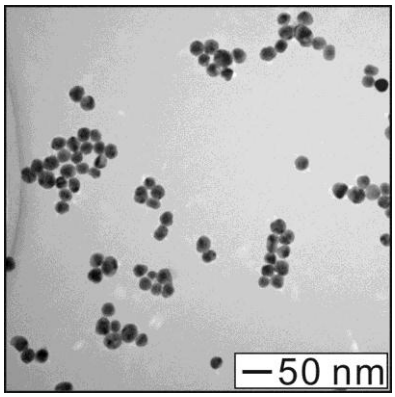

Figure 32

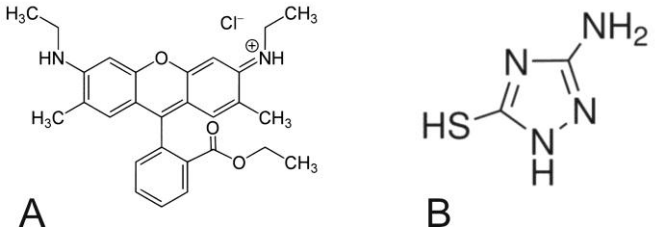

Figure 33

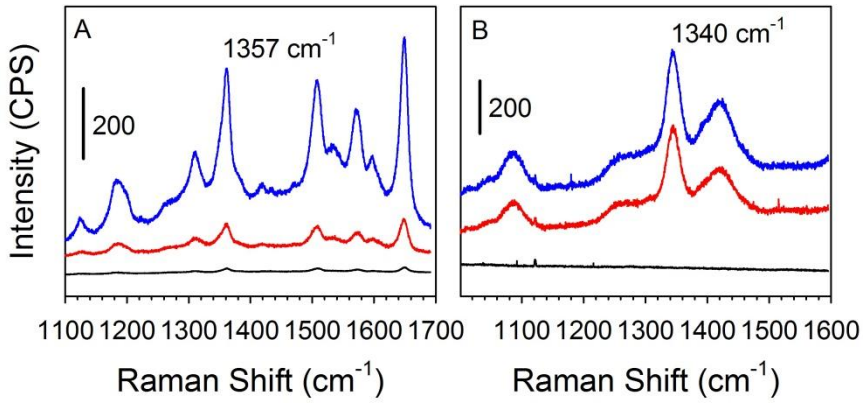

Figure 34

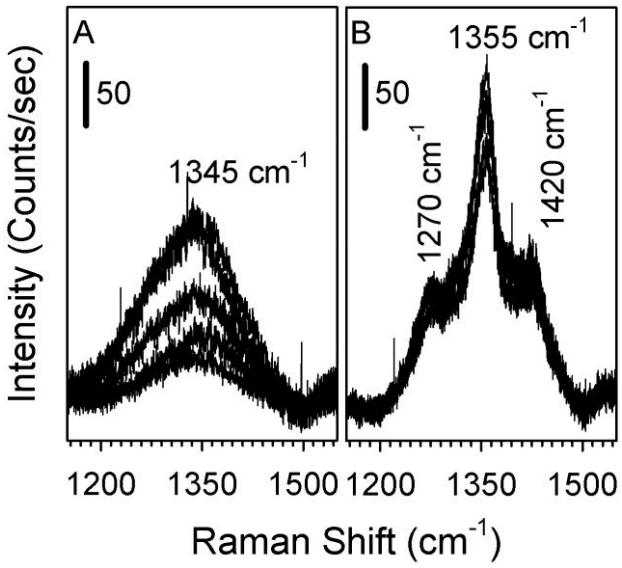

Figure 35

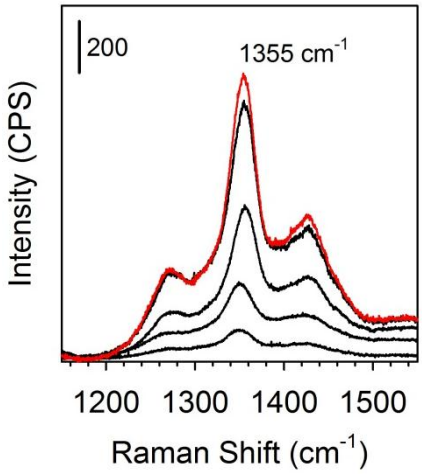

Figure 36